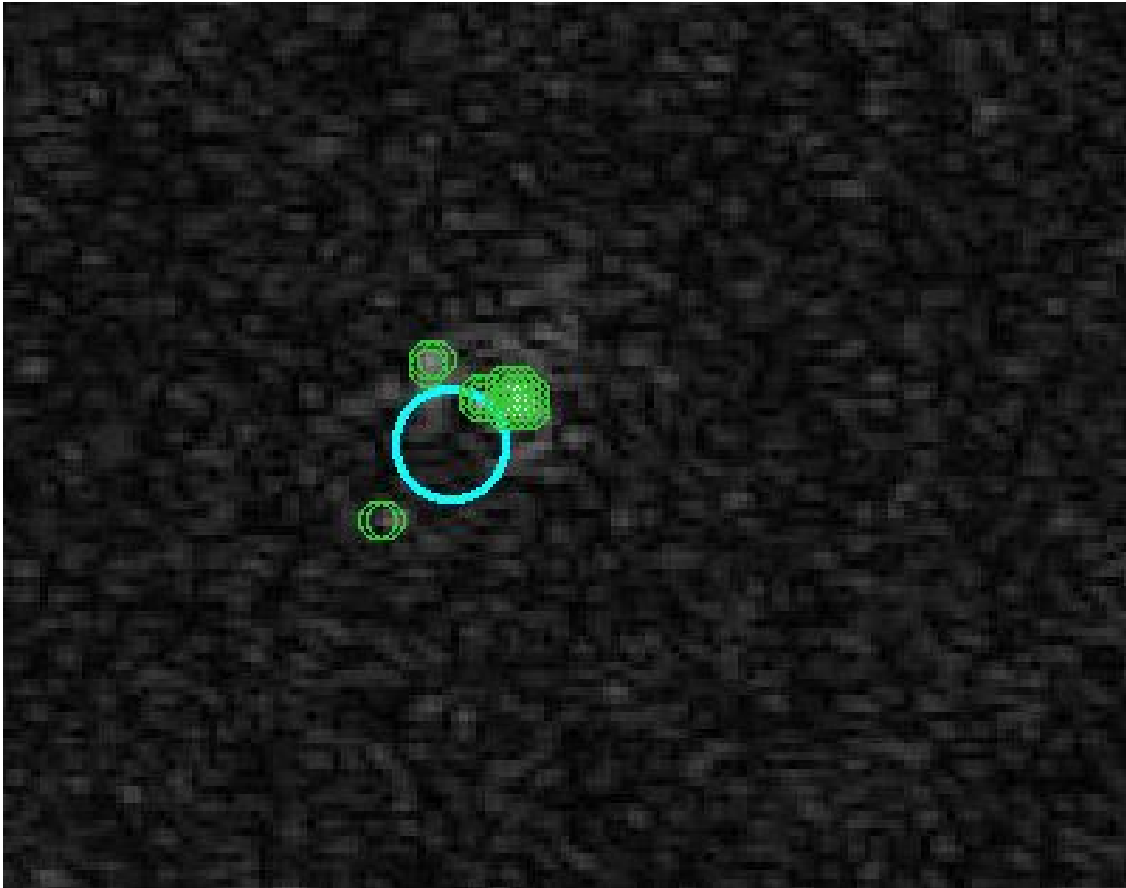




**CHALMERS**  
UNIVERSITY OF TECHNOLOGY

---



## **Search for polarisation in LOFAR data**

Master's thesis in Master Physics and Astronomy

NIKLAS MOSZCZYNSKI



MASTER'S THESIS 2019

# **Search for polarisation in LOFAR data**

NIKLAS MOSZCZYNSKI



Department of Space, Earth and Environment (SEE)  
*Division of Astronomy and Plasma Physics*  
CHALMERS UNIVERSITY OF TECHNOLOGY  
Gothenburg, Sweden 2019

Search for polarisation in LOFAR data  
NIKLAS MOSZCZYNSKI

© NIKLAS MOSZCZYNSKI, 2019.

Supervisor: Prof. Cathy Horellou  
Examiner: Prof. Cathy Horellou

Master's Thesis 2019  
Department of Space, Earth and Environment (SEE)  
*Division of Astronomy and Plasma physics*  
Chalmers University of Technology  
SE-412 96 Gothenburg

Cover: A radio continuum source, found to have four polarised sources marked out with green rings

Printed by Chalmers Reproservice  
Gothenburg, Sweden 2019

Search for polarisation in LOFAR data  
NIKLAS MOSZCZYNSKI  
Department of Space, Earth and Environment  
Chalmers University of Technology

## Abstract

The Low Frequency Array (LOFAR) is a new-generation digital radio telescope centred in the Netherlands and with international stations located in several European countries, including Sweden. The sensitivity, angular resolution, and survey speed of LOFAR makes it an ideal instrument to conduct high-quality observations of the entire northern sky in a poorly unexplored part of the electromagnetic spectrum at frequencies below 180 MHz. LOFAR is anticipated to detect millions of new radio sources. Most of them are extragalactic sources powered by accretion of matter onto supermassive black holes at the centres of galaxies.

LOFAR can detect synchrotron radiation produced by relativistic electrons accelerated by magnetic fields. Measuring the polarisation of the radiation makes it possible to gain insight into the intrinsic properties of the sources and of the magnetised plasma along the line of sight (between the sources and the observer) via Faraday rotation.

In this work, I have analysed data from the ongoing LOFAR survey and developed a new computer code in Matlab to search for polarisation in the large (and rapidly increasing) LOFAR dataset. In the future, it is likely that the use of neural networks will enable significant advances in this type of studies.

**Keywords:** LOFAR, Polarised sources, Synchrotron emission, Faraday rotation, Faraday dispersion function, Faraday cube, LoTSS, Neural networks



## Acknowledgements

There are several people who have helped me during the writing of my thesis, and to whom I owe great thanks: I would like to thank my supervisor, prof. Cathy Horellou for giving me the opportunity to work with this subject. You have helped very much in this project.

I wish to thank Stephen Bourke and Simon Casey for the technical support and the flexibility you both have provided.

I would like to thank also all the people at the Onsala Space Observatory. I enjoyed the pleasant and friendly atmosphere at the Observatory and at Chalmers.

I am grateful that the Swedish National Facility for Radio Astronomy allowed me to participate in one of their meetings.

Finally, I would like to thank my family for their infinite support during the most difficult times writing this thesis. I am very lucky to have my mum, dad and my sister Claudia by my side. They can always find joy and love in my life and they always know how to cheer me up.

Niklas Moszczynski, Gothenburg, June 2019





# Contents

<b>List of Tables</b>	<b>xv</b>
<b>1 A brief introduction to radio astronomy and the LOFAR telescope</b>	<b>1</b>
1.1 Fundamental concepts in Radio astronomy . . . . .	1
1.1.1 Radio waves and radio telescopes . . . . .	1
1.1.2 Interferometry . . . . .	2
1.1.3 Radio galaxies . . . . .	2
1.2 A brief introduction to LOFAR telescope, SKA and the main goal of this project . . . . .	3
<b>2 Physical processes</b>	<b>7</b>
2.1 Synchrotron emission . . . . .	7
2.1.1 Stokes parameters and complex polarisation vector . . . . .	10
2.1.2 Faraday rotation . . . . .	11
2.1.3 Depolarisation and instrumental polarisation . . . . .	13
<b>3 The Faraday dispersion function</b>	<b>15</b>
3.1 Faraday dispersion function . . . . .	15
3.1.1 Derivation of $\tilde{F}(\phi)$ and RMTF . . . . .	15
3.1.2 Rotation measure transfer function . . . . .	19
3.2 Experimental layout . . . . .	21
<b>4 Method for detection of polarised sources in LOFAR data</b>	<b>23</b>
4.1 The LOFAR data . . . . .	23
4.2 Preparation before running the algorithm . . . . .	24
4.2.1 Selecting specific regions in space and constructing Faraday cubes	24
4.2.2 Constructing Faraday cubes . . . . .	25
4.3 Description of the algorithm . . . . .	25
4.3.1 Reading the data . . . . .	25
4.3.2 Detection of radio continuum sources on the intensity map . . . . .	25
4.3.3 Identifying polarised sources and Faraday spectra . . . . .	26
4.3.3.1 Reproduced Faraday spectrum with a specific resolution	26
<b>5 Results</b>	<b>29</b>
5.1 Comparison with the Neld et al. (2018) analysis . . . . .	29
5.2 Region 2 . . . . .	32
5.3 Subfield near source 6 from the article Neld et al. (2018) . . . . .	34

<b>6 Outlook</b>	<b>37</b>
6.1 Discussion of results . . . . .	37
6.1.1 Many polarised sources . . . . .	37
6.2 The code . . . . .	37
6.3 The algorithms consistency with the ds9 . . . . .	38
6.4 Conclusions and outlook. . . . .	38
<b>Bibliography</b>	<b>41</b>
<b>Appendix</b>	<b>I</b>

# List of Figures

1.1	Cygnus A is a large radio galaxy, with a strong double lobe stretching out far more than the size of the galaxy itself, about 92 kpc ( $\sim 300000$ lightyears). The image pictures the galaxy at 4.8 GHz. Source [28] . . . . .	3
1.2	The highlighted dots represent radio telescopes in the LOFAR cooperation. There are 38 Dutch stations and 13 international stations across Europe. Another two stations will come, in Latvia 2019 and in Italy 2022. Source: [27] . . . . .	4
2.1	In a uniform magnetic field the electron spiral around the field lines with the frequency $\nu = eB/2\pi cm_e$ . As the electrons approaches relativistic speeds, $V \longrightarrow c$ the electrons (and if present positrons) will dominate the emission of synchrotron radiation in jets. Synchrotron emission dominates the radio continuum emission from star-forming galaxies like our own at frequencies below $\nu \sim 30\text{GHz}$ . Source [29] . . . . .	7
2.2	The complex polarisation vector in the QU - plane. $\chi$ is the polarisation angle (the position angle of the electric field vector of the wave). . . . .	11
2.3	When the polarised radio emission from a background galaxy passes through a foreground cloud of magneto-ionic gas, the emission undergoes Faraday Rotation. This effect can be detected with a radio telescope, and used to measure the strength of cosmic magnetic fields. In case of the magnetic field $B$ being anti parallel to the direction of propagation of the light, the rotation causes the polarisation to rotate in the mathematical positive direction. . . . .	12
3.1	Normalised Response function, RMTF in a window of Faraday depth between $\phi = -200$ to $200 \text{ rad/m}^{-2}$ for the LOFAR observation of M51. The used bandwidth was 120 MHz to 168MHz with a width of 1MHz for 480 channels (LOFAR HBA). There are almost no visible oscillations which is preferable for studying $\tilde{F}(\phi)$ and accurate detection of polarised sources. The width of the RMTF is $\approx 1 \text{ rad/m}^{-2}$ . . . . .	18
3.2	Absolute value of RMTF for the WSRT (Westerbork Synthesis Radio Telescope). The bandwidth is 315MHz to 370MHz with a width of 1MHz and 480 channels. There are many side lobes which is not favourable for detecting polarised sources. The width of the RMTF is $\approx 1 \text{ rad/m}^{-2}$ . . . . .	19

3.3	In the left panel: A narrow strong peak around $\phi = 0$ and no visible oscillations around 0. In the right panel: The imaginary part of the RMTF for use in LOFAR is almost identical to 0 which is preferable. The used bandwidth was 120 MHz to 168MHz with a width of 1MHz for 480 channels (LOFAR HBA). . . . .	21
3.4	Left hand panel: A graphical presentation of a Frequency cube, consisting of an observed region of sky in multiple frequencies. Right hand panel: A graphical presentation of a Faraday cube. A Faraday cube is the transformed region, from $f$ to $\phi$ space. . . . .	22
4.1	Left panel: Stokes I image of pointing P39Hetdex19 with galaxy in the centre. Right panel: Location of the pointing on the celestial sphere ( $RA \simeq 13h\ 30m$ , $DEC \simeq 47^\circ$ ). . . . .	24
5.1	Faraday spectra for all identified polarised components and sources. . .	31
5.2	The large galaxy is the M51 galaxy. The circles represent polarised sources found by the algorithm. . . . .	32
5.3	Faraday spectra for all identified polarised components and sources. . .	33
5.4	A list of the coordinates from all sources are to be found at the end of the section. The location of source 6 is encircled by the bottom right circle. . . . .	34
5.5	Faraday spectra for all identified polarised components and sources. . .	35
5.6	Source 6 shown in the intensity map observed by LOFAR and FIRST. The cyan coloured circle represents the location of the coordinate for source 6 found in the article [19], the green circles show the location of the identified polarised sources. Left panel: Intensity map observed at 150 MHz with 20'' resolution, dimensions of the image is (right ascension $13^h36^m06^s$ to $13^h36^m27^s$ and declination $48^\circ58'31''$ to $49^\circ02'15''$ ) Right panel: Intensity map observed with FIRST at 1.4 GHz with 5'' resolution. . . . .	36
.1	The image depicts three different networks' possible states for one data set. When the network will have too few layers the network will find and make too few rules which will to that it will not correctly predict the output values for the data set. This is shown under "Underfitting". In the middle image we see a network have too many layers. We see that the network have correctly separated all output values. The problem here is that it is very sensitive for changes and for similar data sets it will not predict correctly. This is called "Overfitting". In the last image we have a nice number of layers. The network has successfully managed to separate the two output values and for some differences it will still be able to separate different output values. One says the network has found the general trend. Figure taken from source: [30] . . . . .	III

- .2 A simplified model of a deep learning neural network. In this task the neural network had, depending on the resolution of the Faraday spectrum, up to 100 neurons. As a standard modelled network there was 20 hidden neurons in each next layer, and there was one output, 1 or 0 (in this figure the output layer have instead four outputs). [30] . . . . . III
- .3 Confusion matrices for both attempts using neural networks for simulated radio polarised data with Ricean noise. The score is perfect. . . . . IV



# List of Tables

5.1	The results from the code applied with the condition $S/N > 6$ . We notice that almost all of the radio continuum sources that have been found to have at least one polarised component have the same Faraday depth as in the referred article, except for source 8 and source 12. Source 8 has a considerable change. The letters in front some of the sources indicate there is more than one polarised component. . . . .	32
5.2	The results presented in the tabular are findings from the code applied with $S/N > 6$ . . . . .	34
5.3	The results presented in the tabular are findings from the code applied with $S/N > 6$ . . . . .	36





# 1

## A brief introduction to radio astronomy and the LOFAR telescope

This chapter will introduce concepts and deal with the basics within radio astronomy.

### 1.1 Fundamental concepts in Radio astronomy

#### 1.1.1 Radio waves and radio telescopes

Knowledge about light that arrives to Earth stands for a big part of our understanding about the Universe. Light is an electromagnetic wave that travels with a speed  $c \approx 3 \times 10^8$  m/s in vacuum. Light with the longest wavelengths are radio waves which are usually defined to have wavelengths  $\lambda_{radio}$  between  $\sim 1$  mm and  $\sim 10$  m and the corresponding frequencies  $f_{radio}$  between 30 MHz and 300 GHz. Light with wavelengths longer than that ( $\lambda \sim 30$  m or frequencies lower than  $f \sim 10$  MHz) cannot be transmitted through the Earth's ionosphere. There are many mechanisms that can be observed through radio waves. In the early age of radio astronomy the pioneers could explore and discover objects such as quasars, radio galaxies and pulsars. Radio waves are however not visible for humans, but they can be detected by radio telescopes. Radio telescopes are collecting (usually weak) radio signals for study of extra-terrestrial sources such as planets, stars and galaxies that are far away. The receivers are therefore built to be very sensitive. The shape usually consists of very large and parabolic formed antennas so that the antenna minimises any reflections and activity, and thus increases the accuracy of obtaining the approaching signal. *Flux* is defined as the power transferred per unit area from the incoming light, and the flux density is flux per unit frequency. The convention used for measuring flux density is in *Jansky*, with  $1 \text{ Jy} = 10^{-26} \text{ W m}^{-2} \text{ Hz}^{-1}$ . The specific intensity is the flux density per solid angle, is also useful and can be expressed as Jy/sr (Jy per steradian), Jy/pix (in a digital image) or Jy/beam (i.e. Jansky per beam area). The angular resolution of the telescope  $\theta$ , is interpreted as the angular distance between two features where they can still be distinguished, which is given by

$$\theta = 1.22 \frac{\lambda}{D} \quad (1.1)$$

where  $\lambda$  is the observed wavelength,  $D$  is the diameter of the antenna and  $\theta$  is the resolution measured in radians.  $D$  is in general called the *aperture diameter* of the telescope. Even the largest radio telescopes with an aperture diameter  $D = 100$  m are limited to  $\theta \gg 1$  arcsec. The strength in radio astronomy is that radio telescopes can

be used together to increase their resolution by increasing their *baseline*, according to eq. (1.1). This technique is called *radio interferometry*. [8]

### 1.1.2 Interferometry

Radio telescopes are usually placed far away from human population, electronic man-made devices and any kind of noise that could disturb observations (electromagnetic interference), for instance on a desert or on open landscapes. Radio telescopes with large distances in between, can benefit from a useful technique called *radio interferometry*, meaning they can achieve greater angular resolution in a group of antennas rather than individually. They simulate an antenna with a larger aperture diameter and increased angular resolution. For a pair of antennas separated by a specific distance (called *baseline vector*  $b$ ), a wave of light will arrive at a separated fixed time-interval. If the direction of the antennas is along the vector  $\hat{r}$  to the distant source, the extra distance that light will have to travel due to the geometric delay will be  $b \cdot \hat{r} = b \cos \alpha$  which is called *projected baseline*, where  $\alpha$  is the angle between the extra distance and the baseline vector. The time-delay will be expressed as  $\tau = b \cdot \hat{r} / c$ . By cross-correlating the signal from the different telescopes (on the principle that waves coinciding with the same phase will add to each other, while two waves that have opposite phases will cancel each other out) gives information about the brightness distribution in the source. This method creates a telescope that is equivalent in resolution (albeit not in sensitivity) to a single antenna whose aperture diameter is equal to the distance of the antennas farthest apart in the array. This technique has already been vastly implemented. [8].

### 1.1.3 Radio galaxies

A radio galaxy is a active galaxy with an active nucleus emitting strongly over the entire electromagnetic spectrum. A significant fraction of the light's intensity from radio galaxies peaks in the radio frequency. The active nucleus is a compact central region of the galaxy in form of a supermassive black hole accompanied with an *accretion disk* along with a single lobe on one side or on both sides of the nucleus. It is suggested that a supermassive black hole is powered by matter losing gravitational potential energy in the accretion disk around them. To understand this powerful engine one can follow this argument. When mass is falling freely it will gain kinetic energy in exchange for potential energy. Matter falling onto some body is termed accretion. Eventually the kinetic energy will be released as heat, and appear in some form of radiation. The *luminosity*  $L$ , is defined as the power from electromagnetic waves from an emitting object (radiant power) and it can be expressed through the energy relation,  $L = \frac{1}{2} \frac{dm}{dt} v_{ff}^2 = \frac{GM \frac{dm}{dt}}{R}$ . Here  $\frac{dm}{dt}$  stands for the mass rate,  $G \approx 6.67 \times 10^{-11} \text{ m}^3 \text{ kg}^{-1} \text{ s}^{-2}$  and  $v_{ff}$  stands for the velocity of free fall of the matter flowing in. All matter that falls within the Schwarzschild radius  $r_s$  cannot send a signal to the outside of the world anymore (the Schwarzschild radius,  $r_s = 2GM/c^2$  for a spherical non-rotating black hole). Using the expression for  $r_s$  one can plug in and show that the luminosity of the accretion is  $L = \frac{1}{2} \frac{dm}{dt} c^2 \frac{r_s}{R}$  and in general  $L = \zeta \frac{dm}{dt} c^2$ . In this form  $\zeta$  can be seen to be the efficiency of the conversion of rest mass energy into luminos-

ity. The efficiency of the energy conversion of matter falling in to the accretion disk of black holes is huge. It is only dependent on the radius of the black hole and the Schwarzschild radius,  $\zeta = \frac{1}{2} r_s/R$ , which can also be put that it is dependent on the density of the black hole, which we know is very dense. [7]

Radio galaxies differ very much when it comes to size and luminosity, which for instance depends on the speed and length of the jets. A useful system, radio galaxies are categorised by the Fanaroff-Riley (FR) classification where there are two classes, FRI and FRII. FRI objects typically have bright jets in the centre, while FRIIs have faint jets but bright hotspots at the ends of the lobes. FRIIs appear to be able to transport energy efficiently to the ends of the lobes, while FRI beams are inefficient in the sense that they radiate a significant amount of their energy away as they travel. The theory of jets is not complete but it is presumed that magnetic fields play an important role for the collimation of jets. Weak jets are a few parsec long and travel at around 10 % of speed of light, while the most extreme and violent jets could be up to tens or hundreds of kpc long and move close to the speed of light (1 parsec, for short pc, is 3.26 light years) [23], [11]. See for instance fig.1.1, the Cygnus A which is a radio galaxy.

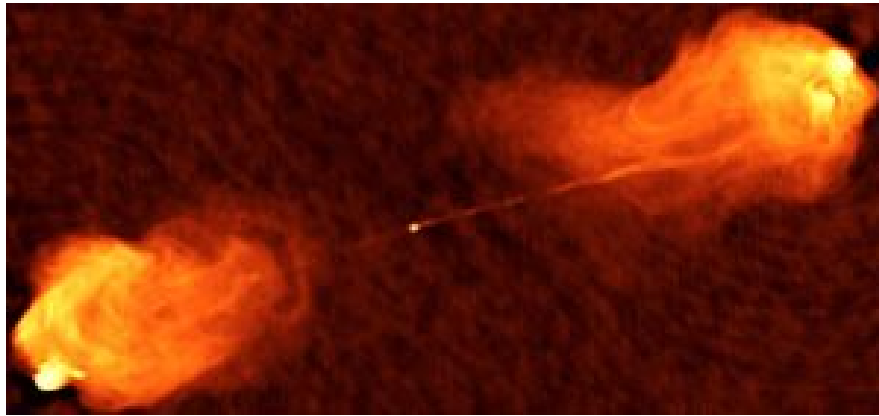


**Figure 1.1:** Cygnus A is a large radio galaxy, with a strong double lobe stretching out far more than the size of the galaxy itself, about 92 kpc ( $\sim 300000$  lightyears). The image pictures the galaxy at 4.8 GHz. Source [28]

## 1.2 A brief introduction to LOFAR telescope, SKA and the main goal of this project

The LOw Frequency ARray, LOFAR, is a new-generation digital radio telescope and one of the largest radio telescopes in the world, it offers a huge increase in radio survey speed compared to existing radio telescopes. LOFAR is operating in the radio frequency range, within two frequency bands, (20-80 MHz and 120-180 MHz), centred in the Netherlands with several international stations including in France, Germany, the United Kingdom, Poland and Sweden in Onsala with baselines from 100 m to 1500 km, see fig. 1.2.

LOFAR is an aperture synthesis array composed of phased array stations. Each station consists of an array of dipoles, functioning as antennas. In total there are 51 stations

and 8000 antennas. There are three kinds of LOFAR stations with individual characteristics which, according to their distance from the centre of the array, are classified as Core, Remote and International stations. The three kinds of stations have different antenna field configurations and underlying electronics. Currently, LOFAR consists of 24 Core stations, around Exloo in the Netherlands, 14 Remote stations distributed over the Netherlands and 13 International stations distributed over Europe. LOFAR post-processing of data can take place either at the Central Processor in the Netherlands or locally with the users. If the available Internet capacity is sufficiently good, intermediate data products can be transported to the user, and local processing can be done. Otherwise processing resources at the Central Processor are available for further data reduction (within the limits of the Central Processor processing capacity). [24], [1]

Much of the work with LOFAR is organised in so-called Key science projects (KSP). In the Magnetism KSP (the MKSP<sup>1</sup>), researchers study magnetic fields in the universe by observing polarised synchrotron emission with LOFAR. Faraday screens and rotation measure synthesis/Faraday tomography is used to investigate the 3-D structure of local magnetic fields in the Milky Way which probes the magneto-ionic structure of the very local ISM surrounding the Sun. Moreover the International Key Science Project "Cosmic Magnetism" is divided into further smaller groups with a total of 85 members and 6 groups, where the author was a part of one group called "RM Grid Task Force" which is focusing on detecting extragalactic polarised sources. Polarised radio emission has been observed in jets and lobes of several radio galaxies. A specific galaxy that has been of big focus for investigation was M51, also called the whirlpool galaxy. [14]



**Figure 1.2:** The highlighted dots represent radio telescopes in the LOFAR cooperation. There are 38 Dutch stations and 13 international stations across Europe. Another two stations will come, in Latvia 2019 and in Italy 2022. Source: [27]

---

<sup>1</sup><http://www.lofar.org/astronomy/cosmic-magnetism/cosmic-magnetism>

LOFAR is a pathfinder for the SKA (Square Kilometer Array) in centimetre and metre wave radio astronomy (initially from frequencies 50 MHz to 15 GHz, and likely extending to 24 GHz), with dishes in South Africa and Australia. This will make the SKA the largest radio telescope array ever constructed, which will be an enormous array of antennas with a "lifespan" of at least 50 years, in other words stretching into the 2070's. The total collecting area of the SKA will be well over one square kilometre and with wider frequency range it will increase the angular resolution. It is calculated to have an impressive resolution of milliarcseconds. It will offer new interesting possibilities for a wide range of studies, for example

- Probing the Cosmic Dawn and the Epoch of Reionization
- Galaxy Evolution, Cosmology, and Dark Energy
- Strong-field Tests of Gravity using Pulsars and Black Holes
- The Origin and Evolution of Cosmic Magnetism
- Sign of Life
- The unknown

The building is still in progress, and first science is expected in the early 2020s. [20]



# 2

## Physical processes

### 2.1 Synchrotron emission

*Synchrotron emission* is a type of radiation caused by a charged particle being accelerated or decelerated due to a magnetic field to very high (ultra relativistic) velocities. The acting magnetic force is the Lorentz force acting perpendicular to the electron's velocity. The emission is also called Magnetobremstrahlung from the German translation meaning "Magnetic braking radiation". Sources of synchrotron emission are located for instance in magneto-ionised mediums in jets in radio galaxies, for illustration of the phenomena see fig. 2.1.

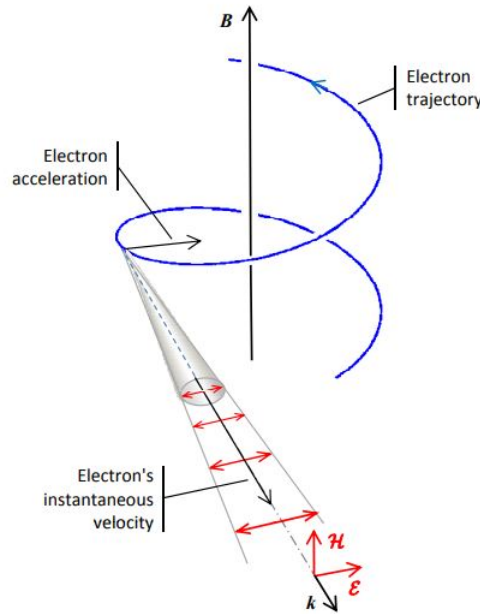


**Figure 2.1:** In a uniform magnetic field the electron spiral around the field lines with the frequency  $\nu = eB/2\pi c m_e$ . As the electrons approach relativistic speeds,  $V \rightarrow c$  the electrons (and if present positrons) will dominate the emission of synchrotron radiation in jets. Synchrotron emission dominates the radio continuum emission from star-forming galaxies like our own at frequencies below  $\nu \sim 30\text{GHz}$ . Source [29]

Synchrotron emission represents a significant portion of radiation from radio galaxies and it accounts for most of the radio emission from active galactic nuclei (AGN). The synchrotron emission from the lightest particles (electrons and if present positrons) in jets is ubiquitous and stands for almost all synchrotron radiation reaching Earth. The Lorentz force from a magnetic field acting on an electron is defined as

$$\mathbf{F} = \frac{e(\mathbf{v} \times \mathbf{B})}{c}$$

The Lorentz force is acting perpendicular to the electron's velocity, so we have that  $\mathbf{F} \cdot \mathbf{v} = 0$ . The electrons are moving in spiral paths along the magnetic field and the velocity component of the electron parallel to the magnetic field will not change over time. This means that the total velocity  $|\mathbf{v}|$  remains constant over time and that the electron's kinetic energy is conserved. What happens is that the electron's velocity is changing direction. [18]

We consider the power for the emission from a classically moving electron in a magnetic field, using Larmor's power formula. The formula describes the power due to acceleration or deceleration from the Lorentz force acting on a free charged particle. For a slow and non-relativistic electron we have,

$$P = \frac{2e^2 a_{\perp}^2}{4\pi\epsilon_0 c^3}. \quad (2.1)$$

In jets there are mostly (ultra) relativistic electrons, and most astronomical relativistic sources are not in local thermal equilibrium so they don't follow a Maxwellian velocity distribution, they follow a power-law. The synchrotron sources are sometimes also called non-thermal sources. [8]

Effects in special relativity becomes relevant and must be taken into account for ultra relativistic electrons. Time, velocity and acceleration are dependent in which frame one is considering. In the frame of electrons moving relativistically  $P'$  (the power) will have a different expression from eq. (2.1) since the acceleration will change in the inertial frame of the electrons (it is the only quantity that will change). The best frame to consider the electron is in polar (in 3 dimensions cylindrical) coordinates which yields that the acceleration is pointing radially. We must however convert from a polar coordinate system to a Cartesian coordinate system  $a_{\perp}^2 = a_x^2 + a_y^2$ . From the theory of special relativity we write the acceleration in the following way  $\frac{dv_x}{dt} = \frac{dv_x}{dt'} \frac{dt'}{dt} = \frac{1}{\gamma} \frac{dv'_x}{dt'} \frac{dt'}{dt} = \frac{1}{\gamma^2} a'_x$ . The acceleration in one direction is scaled by the Lorentz factor<sup>2</sup>. Summarised this yields

$$a_{\perp} = \frac{a'_{\perp}}{\gamma^2}$$

which gives by insertion in eq. (2.1)

$$P' = \frac{2e^2 a_{\perp}'^2 \gamma^4}{4\pi\epsilon_0 c^3} \quad (2.2)$$

A similar reasoning yields that the power is invariant under Lorentz transformation, i.e.  $P' = P$ . The radial (centripetal) acting force on the electron is written in scalar form  $a_{\perp} = \omega v_{\perp}$ , where  $\omega v_{\perp} = \frac{eBv_{\perp}}{\gamma m_e c} = \frac{eBv \sin \alpha}{\gamma m_e c}$ . The angle  $\alpha$  is called the *pitch angle*



which is a constant angle between the velocity of the electron and the magnetic field. It is a constant angle because the centripetal acceleration, depends on the total velocity which has been shown before, to be constant and no other quantity is changing. Inserting the expression for the centripetal acceleration in equation (2.2) yields the final result for power of an individual relativistic electron. A perhaps more interesting quantity is to calculate the average of the radiated power from synchrotron emission per relativistic electron in an ensemble,

$$\langle P \rangle = 2\sigma_T c U_B \gamma^2 \beta^2 \langle \sin^2(\alpha) \rangle \quad (2.3)$$

where  $\sigma_T$  is the Thomson scatter cross-section, which is the classical radiation-scattering cross section of a charged particle, so  $\sigma_T \approx 6.65 \times 10^{-25} \text{cm}^2$ .  $U_B = B^2/8\pi$  is the magnetic energy density. For an ensemble of electrons, the distribution of their pitch angles  $\alpha$ , will gradually become random and isotropic. The total radiated power from an ensemble of (ultra) relativistic electrons is

$$\langle P \rangle = \frac{4}{3} \beta^2 \sigma_T c U_B \gamma^2 \quad (2.4)$$

where  $\langle \sin^2(\alpha) \rangle = 2/3$ . [8].

The energy distribution of relativistic electrons in most synchrotron sources follows roughly a power-law:

$$n(E)dE = E^{-\delta} dE \quad (2.5)$$

where  $n(E)dE$  is the number of electrons per unit volume with energies from  $E$  to  $E + dE$ . For an ensemble of electrons one observes their spectrum follow a power law.

$$I_\nu \propto \nu^{-\alpha} \quad (2.6)$$

$\nu$  is the frequency and  $I_\nu$  is the specific intensity. The spectral index  $\alpha$  is defined as the logarithmic slope of the power spectrum of,  $\alpha \equiv \frac{d \log P_\nu}{d \log \nu}$  (not to be confused with the pitch angle). In the Milky Way and most astrophysical sources of synchrotron radiation (such as radio lobes) have spectral indices near  $\alpha \approx 0.75$ .  $\alpha$  depends only on  $\delta$

$$\alpha = \frac{\delta - 1}{2} \quad (2.7)$$

$\alpha \approx 0.75$  yields  $\delta \approx 2.5$ .

Synchrotron emission is partially polarised, and one can hypothetically calculate the *intrinsic degree of polarisation* from synchrotron polarisation from plasma in a uniform magnetic field according to

$$\|p\| = \frac{3\delta + 3}{3\delta + 7} \quad (2.8)$$

In practice the degree of polarisation is usually lower than the theoretical due to depolarisation effects, which means the light becomes polarised more than once along the line of sight, an additional effect discussed later on. The theoretical limit of the degree of polarisation for the given examples has been calculated to about 72%.

Nevertheless electrons cannot continue this process forever due to energy losses through synchrotron radiation. To calculate how fast an average electron is losing energy, the electron's energy corresponding to the rest mass  $E = \gamma m_e c^2$  will be gone after

$$t_{1/2} = \frac{E}{2} \left| \frac{dt}{dE} \right| \quad (2.9)$$

Thus the half-life is proportional to  $B^{-1/2}$  and so we can write

$$t_{1/2} \approx 34 \left( \frac{10^{-5} G}{B} \right)^{3/2} \left( \frac{10^9 \text{ Hz}}{\nu} \right)^{1/2} \quad (2.10)$$

For fields of  $10^{-5} G$  that are believed to be typical in radio lobes, the life of electrons emitting at 5 GHz is about 10 millions years. [23].

### 2.1.1 Stokes parameters and complex polarisation vector

There is a set of parameters that makes it convenient to study polarisation of light. The parameters are called Stokes parameters after George Gabriel Stokes who first used them and they describe the intensity and the polarisation of light. There are four Stokes parameters,  $I, Q, U$  and  $V$ .  $I$  represents the intensity of light while  $Q$  and  $U$  represent the linearly polarised part of light and in case of a circular polarisation, a fourth parameter is introduced  $V$ . Synchrotron radiation is a linearly polarised wave, which results in that three Stokes parameters are needed  $I, Q$  and  $U$  to fully describe light. When studying *Faraday rotation* (which will be discussed in the next section) it is common to introduce the complex vector,  $P = Q + iU$  called the *complex polarisation vector* or *complex polarised surface brightness*, a superposition of the linearly polarised parameters  $Q$  and  $U$ . The complex polarisation vector is represented by the Stokes parameters in a coordinate system where  $Q$  and  $U$  are represented along axes. The length of the complex polarisation vector is called the *total polarised intensity* which is calculated  $|P| = \sqrt{Q^2 + U^2}$ . [3]. The angle that the complex polarisation vector makes with the  $Q$  - axis is the *polarisation angle*,  $2\chi$ . The polarisation angle is obtained from the Stokes parameters accordingly

$$2\chi = \tan^{-1}(U/Q) \quad (2.11)$$

The factor 2 comes from a so-called  $\pi$  - ambiguity since there's no difference in observation if the angle is rotated an additional 180 degrees or a multiple of that compared being not rotated at all. In regards to synchrotron emission, the complex vector can also be written as  $\mathbf{P} = |P|e^{2i\chi}$ . The geometrical representation is found in fig. 2.2.

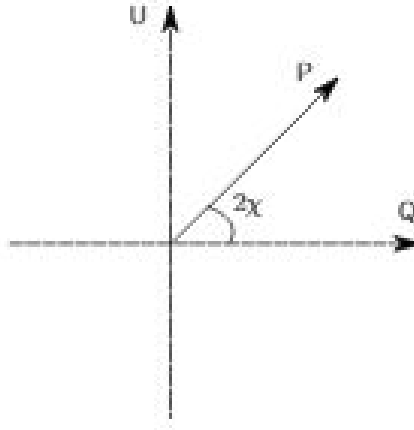


**Figure 2.2:** The complex polarisation vector in the QU - plane.  $\chi$  is the polarisation angle (the position angle of the electric field vector of the wave).

### 2.1.2 Faraday rotation

When synchrotron emission travels through a magneto-ionised medium, the polarisation angle of light becomes altered. This effect is called *Faraday rotation* or *Faraday effect* after the British physicist Michael Faraday and it is sketched in fig. 2.3. The rotation of the polarisation angle from the passing light, is due to *circular birefringence* which is the induced effect of Faraday rotation that only rotates the orientation of a wave's linear polarisation. The polarisation angle will rotate in the mathematical negative direction if the magnetic field direction is oriented parallel to the line of sight, or it will rotate in the mathematical positive direction in the case of an anti parallel orientation of the magnetic field. The total angular difference depends on the total electron density in the magneto-ionised medium and also on the length of the path of light is passing through the magneto-ionised medium. The equation describing how the polarisation angle  $\chi$  changes after passing a magneto-ionised medium as a function of the parameters given above is given in the following eq. (2.12).

$$\Delta\chi \approx 0.812 \int_0^d n_e B_{\parallel} \lambda^2 ds \quad (2.12)$$

where  $\Delta\chi$  is the total change in polarisation angle after the synchrotron emission had passed through the medium. The variable  $n_e$  denotes the total electron energy density and  $B_{\parallel}$  denotes for the component of the magnetic field parallel to the observer. The integral goes over the distance of which light had travelled through the magneto-ionised medium. We see that it also depends on the wavelength<sup>2</sup> ( $\lambda^2$ ). This means that the change in polarisation angle increases as the wavelength increases.

Today this effect is an important asset and it is used in observations to detect radio waves from extra galactic polarised sources. This becomes beneficial when studying polarised sources in the radio frequency due to the long wavelength.

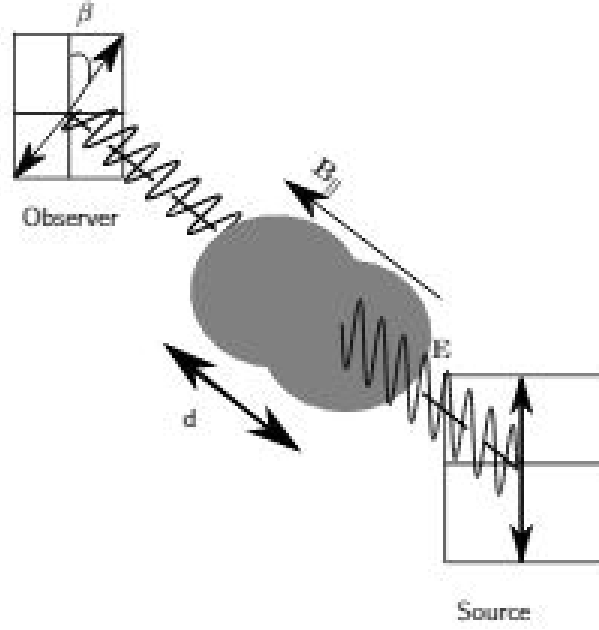


**Figure 2.3:** When the polarised radio emission from a background galaxy passes through a foreground cloud of magneto-ionic gas, the emission undergoes Faraday Rotation. This effect can be detected with a radio telescope, and used to measure the strength of cosmic magnetic fields. In case of the magnetic field  $B$  being anti parallel to the direction of propagation of the light, the rotation causes the polarisation to rotate in the mathematical positive direction.

The observed or measured change in polarisation angle is called *rotation measure*, and it is commonly defined as the slope of the polarisation angle over  $\lambda^2$ ,  $\mathbf{RM} = \frac{d\chi(\lambda^2)}{d\lambda^2}$  (where  $\mathbf{RM}$  is for short rotation measure). It can be established that

$$\chi = \chi_0 + \mathbf{RM}\lambda^2 \quad (2.13)$$

where  $\chi$  is the polarisation angle measured at the wavelength of observation  $\lambda$ ,  $\chi_0$  is the polarisation angle before light enters the magneto-ionised medium. However for measurements the rotation measure is calculated as

$$\mathbf{RM} = \frac{\chi_2 - \chi_1}{\lambda_2^2 - \lambda_1^2}. \quad (2.14)$$

For Faraday rotation, in case of when there is only one source along the line of sight (*los*) with no internal Faraday rotation and also so called no *beam depolarisation* (non-emitting foreground medium) the eq. (2.12) is used as a model that can be also written in the following way

$$\chi(\lambda^2) = \chi_0 + \lambda^2 \phi(\mathbf{r}) \quad (2.15)$$

The variable  $\phi(\mathbf{r})$  is the so-called *Faraday depth* which is a physical quantity defined as,

$$\phi(\mathbf{r}) \approx 0.812 \int_0^d n_e \mathbf{B} \cdot d\mathbf{r}. \quad (2.16)$$

Under these circumstances, the rotation measure will exactly equal the Faraday depth,  $\text{RM} = \phi$ . [3].

### 2.1.3 Depolarisation and instrumental polarisation

In some cases there can occur depolarisation. The different effects of depolarisation can be explained by vector summation of polarisation vectors in the  $Q - U$  plane. The resultant vector from all sources becomes the observed polarisation vector. This can occur because of the beam depolarisation, bandwidth depolarisation or Faraday depolarisation.

- *Beam depolarisation* is when the changing polarisation components are along various lines of sight, but still within the telescope beam.
- In case if many channels are averaged or if a frequency channel is wide enough, the polarisation angle may vary within the channel to develop depolarisation. This affects high RM and long wavelengths more. This is called *bandwidth depolarisation*.
- In case of *Faraday depolarisation*, an observer will see contributions from all of its Faraday depths if it is extended along the line of sight for a structure that is both emitting and Faraday rotating. Even if the polarisation is coherent at different depths, the fact that light will be rotated means that emission from different depths will be differently polarised, and as such depolarisation will occur. This effect is stronger at longer wavelengths.

One important issue found in many other observations, is the *instrumental polarisation* or sometimes called leakage. This happens when the total intensity spills over into  $Q$  and  $U$  parameters. Noise in total intensity also contributes somewhat to the noise in  $\phi$  - space through this mechanism and it is not frequency dependent except in so far as  $I$  is [3]. This must be taken into account when studying polarised sources.



# 3

## The Faraday dispersion function

### 3.1 Faraday dispersion function

In the study of Faraday rotation and polarised sources, an important object needs to be introduced, called the *complex Faraday dispersion function*. The Faraday dispersion function  $F(\phi)$  is dependent on the Faraday depth,  $\phi$  (earlier encountered in eq. (2.16)) and it is the complex polarised surface brightness per unit Faraday depth. The Faraday dispersion function has a tight relationship with the complex polarisation vector  $P(\lambda^2)$ , which is now a function of the wavelength<sup>2</sup>, through the integral transform

$$P(\lambda^2) = \int_{-\infty}^{+\infty} F(\phi) e^{2i\phi\lambda^2} d\phi \quad (3.1)$$

The integral transform in eq. (3.1) is similar to the Fourier transform, however there exists a fundamental difference between the Fourier transform and this integral transform.  $P(\lambda^2)$  is only defined for  $\lambda^2 > 0$  because no measurements can be made at wavelengths less than zero. All values of  $\lambda^2 < 0$  are nonphysical. The integral is only invertible if one makes some assumptions on the value of  $P$  at  $\lambda^2$ . An example is that  $P$  is Hermitian which corresponds to that  $F(\phi)$  is strictly real (Brentjens M.A & de Bruyn A.G 2005).  $Q(\lambda^2)$  and  $U(\lambda^2)$  are Gaussian distributed so from their relation  $P(\lambda^2)$  is a Rician distribution<sup>1</sup>. The integral transform will lead to that it keeps the shape, which also makes it a Rician distribution [17]. A Faraday dispersion function (Faraday spectrum) will usually contain a lot of noise in the Faraday space ( $\phi$ ), and in some cases having one large peak/spike (signal). The function tells if there is a polarised source and the characteristics of the Faraday dispersion function will be investigated more deeply and presented in the report.

#### 3.1.1 Derivation of $\tilde{F}(\phi)$ and RMTF

In the previous subsection we subconsciously introduced the Faraday dispersion function for ideal observations. In real observations one is limited to a certain bandwidth where one measures at discrete frequencies/wavelengths. The goal of this subsection is to derive the approximate Faraday dispersion function  $\tilde{F}(\phi)$  that will correspond to the strongest signal detection accuracy (maximising the signal to noise ratio,  $S/N$ )

---

<sup>1</sup>The noise is a Rician distribution which is a distribution of the norm of two normally distributed variables. Specifically, this distribution models line of sight scatter, such as radio waves transmissions, between two sources in view of each other that have an unobstructed path between them

### 3. The Faraday dispersion function

---

<sup>2</sup>, due to the interesting new object (filter) abbreviated RMTE.

In case of a traditional Fourier transformation the exact inverted relation of eq. (3.1) would look something like this

$$F(\phi) = \frac{2}{\pi} \int_{-\infty}^{+\infty} P(\lambda^2) e^{-2i\phi\lambda^2} d\lambda^2 \quad (3.2)$$

From before we know that this transformation is however ineligible because of lack of measurements for  $\lambda^2 < 0$ . In real observations one is also limited to measure at selected frequencies/wavelengths. Therefore one introduces a sample function/weight function  $W(\lambda^2)$ , which is defined as

$$\begin{cases} W(\lambda^2) = 1, & \text{measurements taken} \\ W(\lambda^2) = 0, & \text{otherwise} \end{cases}$$

When there are no measurements the weight function is zero. The complex polarisation vector can be related to the Faraday dispersion function through a sum incorporated with a weight function. We redefine our polarisation function as

$$\tilde{P}(\lambda^2) = W(\lambda^2)P(\lambda^2) \quad (3.3)$$

This object is exactly what one gets out of observations which is called *observed polarised flux density* or *surface brightness*. We can now carry out the weight function in eq. (3.1)

$$\tilde{P}(\lambda^2) = W(\lambda^2) \int_{-\infty}^{+\infty} F(\phi) e^{2i\phi\lambda^2} d\phi. \quad (3.4)$$

In order to proceed for the approximated Faraday dispersion function one defines now the following function RMTE dependent on  $\phi$ ,

$$R(\phi) = \frac{\int_{-\infty}^{+\infty} W(\lambda^2) e^{-2i\phi\lambda^2} d\lambda^2}{\int_{-\infty}^{+\infty} W(\lambda^2) d\lambda^2} \quad (3.5)$$

which is normalised to unity at  $\phi = 0$ . This function has information about the observations, but not about the value of the signal. The full name of  $R(\phi)$  in eq. (3.5) is called *Rotation Measure Transfer Function* or sometimes *Rotation Measure Spread Function* (RMTE/RMSF). The expression of the RMTE corresponds to the optimal linear filter for maximising the signal to noise ratio, according to the matched filter theorem in one dimension [12]. If we convolve  $F(\phi)$  with  $R(\phi)$  we obtain  $F(\phi) * R(\phi) = \tilde{F}(\phi)$  (where  $*$  denotes convolution),

$$\tilde{F}(\phi) = \frac{\int_{-\infty}^{+\infty} \tilde{P}(\lambda^2) e^{-2i\phi\lambda^2} d\lambda^2}{\int_{-\infty}^{+\infty} W(\lambda^2) d\lambda^2}. \quad (3.6)$$

---

<sup>2</sup>In spectrum analysis a common and good measurement of finding peaks is the *signal to noise ratio*, for short  $S/N$ , which is the quotient of the value of a single peak/signal ( $S$ ) to the value of the noise ( $N$ ) of the spectrum. The noise has the value of the standard deviation of the spectrum  $\sigma$ , the value of the peak is expressed through  $\mu + n\sigma$  where  $\mu$  is the mean of the spectrum, and  $n$  is uniquely determined through the value of the peak or in other words,  $S/N > n$



$\tilde{F}(\phi)$  is the approximate reconstruction of  $F(\phi)$ . The role of  $R(\phi)$  is analogous to the Point Spread Function (PSF) in aperture synthesis. The imperfections in the coverage results in what sometimes is called "dirty" Faraday dispersion function, analogous to the dirty image in aperture synthesis. The quality of the reconstruction depends mainly on the weight function  $W(\lambda^2)$  and the sampling of  $\lambda^2$ . A more complete coverage of  $\lambda^2$  improves the reconstruction. Less holes in the set of  $\lambda^2$  reduces the side lobes of  $R(\phi)$  and covering a larger space of  $\lambda^2$  increases the resolution in  $\phi$  space. In more real situations one must take into account that channels have a finite bandwidth and channel bandpass. This is sometimes approximated with that the bandpass is assumed to be a top hat channel or a sinc. The integrals (3.5) and (3.6) becomes more realistically described as a sum,

$$\begin{cases} \tilde{F}(\phi) \approx K \sum_{i=1}^N \tilde{p}_i e^{-2i\phi\lambda_i^2} \\ R(\phi) \approx K \sum_{i=1}^N w_i e^{-2i\phi\lambda_i^2} \\ K = (\sum_{i=1}^N w_i)^{-1} \end{cases} \quad (3.7)$$

By deconvolution of the integral in (3.6) we will obtain  $F(\phi)$ , which would in terms of image processing correspond to "clean". This process of extracting  $F(\phi)$  is called RM - synthesis. [3]

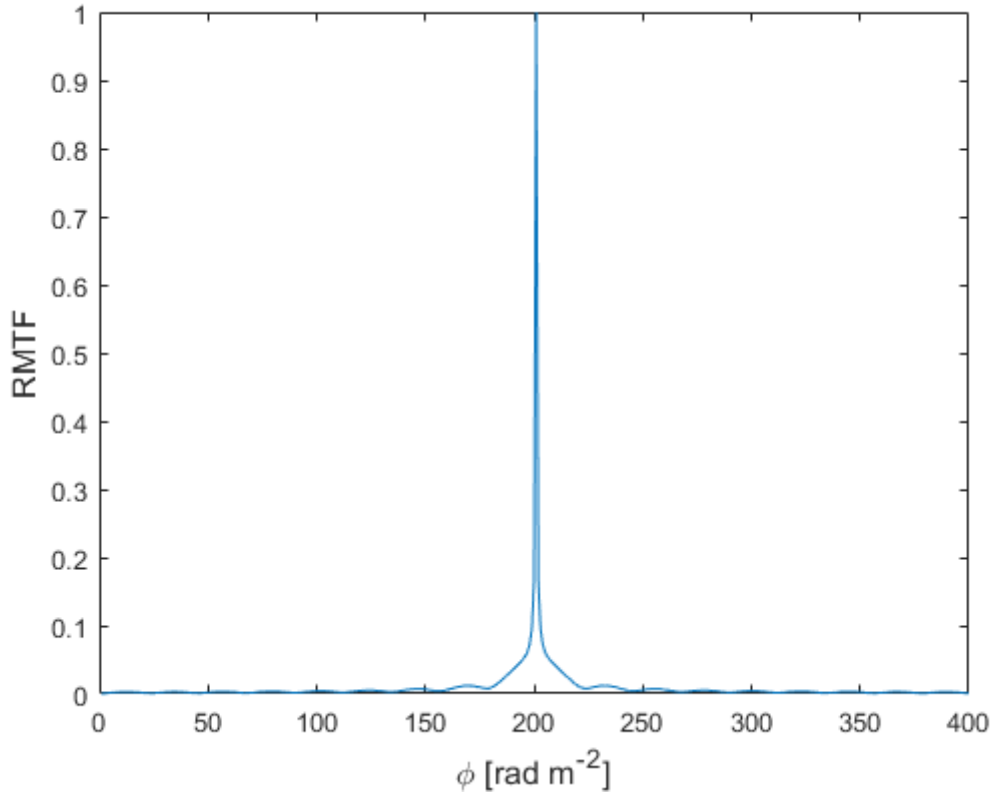


**Figure 3.1:** Normalised Response function, RMTF in a window of Faraday depth between  $\phi = -200$  to  $200 \text{ rad/m}^{-2}$  for the LOFAR observation of M51. The used bandwidth was 120 MHz to 168MHz with a width of 1MHz for 480 channels (LOFAR HBA). There are almost no visible oscillations which is preferable for studying  $\tilde{F}(\phi)$  and accurate detection of polarised sources. The width of the RMTF is  $\approx 1 \text{ rad/m}^{-2}$ .

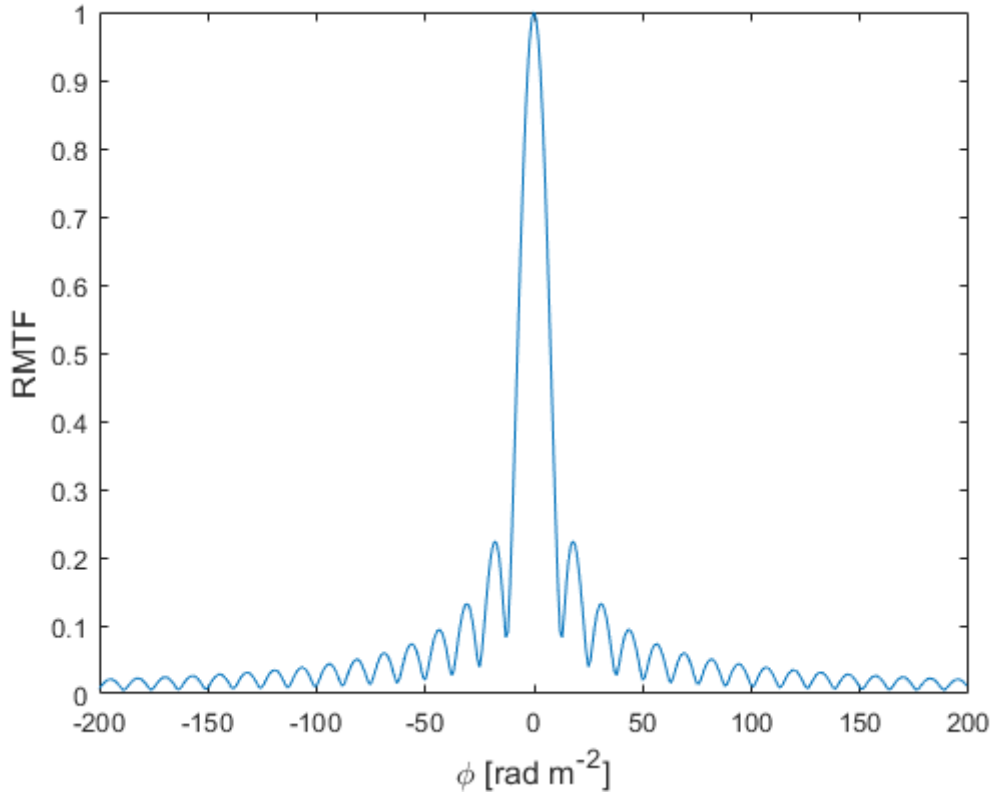


**Figure 3.2:** Absolute value of RMTF for the WSRT (Westerbork Synthesis Radio Telescope). The bandwidth is 315MHz to 370MHz with a width of 1MHz and 480 channels. There are many side lobes which is not favourable for detecting polarised sources. The width of the RMTF is  $\approx 1 \text{ rad/m}^{-2}$

### 3.1.2 Rotation measure transfer function

RMTF is a complex function although the main interest, when studying polarised sources, is the absolute value of RMTE,  $\sqrt{Im(R(\phi))^2 + Re(R(\phi))^2}$ . When  $\phi$  is close to zero the response function displays a rapid developing behaviour and oscillations which makes it difficult to determine the value for any  $F(\phi)$ . One wishes to decrease these oscillations. When the oscillations drops, the accuracy to determine  $F(\phi)$  grows. The current expression, for the approximated reconstruction of  $F(\phi)$ ,  $\tilde{F}(\phi)$  and RMTE in eq. (3.6) and in eq. (3.5) corresponds to derotating all polarisation vectors back to their position at  $\lambda^2 = 0$  before any Faraday rotation has occurred. This might sound there is no reason for further investigation, however derotating to any other  $\lambda_0^2 \neq 0$  does not mean any information will be lost. This is a consequence of the shift theorem in Fourier analysis.

$$\tilde{F}(\phi) = \frac{\int_{-\infty}^{+\infty} \tilde{P}(\lambda^2) e^{-2i\phi(\lambda^2 - \lambda_0^2)} d\lambda^2}{\int_{-\infty}^{+\infty} W(\lambda^2) d\lambda^2} \quad (3.8)$$

$$R(\phi) = \frac{\int_{-\infty}^{+\infty} W(\lambda^2) e^{-2i\phi(\lambda^2 - \lambda_0^2)} d\lambda^2}{\int_{-\infty}^{+\infty} W(\lambda^2) d\lambda^2} \quad (3.9)$$

### 3. The Faraday dispersion function

---

Because the shift theorem tells us that only the argument will be affected and consequently the amplitude of RMTF remains constant. This means that all oscillations and side lobes will remain the same and no change in the argument shift can make a change in the oscillations which makes sense, since it should only depend on the sampling of  $\lambda^2$ .

However shifting the argument a constant value does have an impact on the complex RMTF. The intuition behind the matched filters relies on the scalar product in geometry and correlating the received signal with the filter that is parallel with the signal (real part of RMTF), that maximises the inner product and enhances the signal. When one considers the noise, the additional challenge is of minimising the output by choosing a filter that is orthogonal (imaginary part of RMTF) to the noise. The real part of RMTF is responsible for the parallel response of the transform at the constant value  $\lambda_0$  while the imaginary part accounts for the orthogonal response. In the entire main peak we would like to have a response parallel to the polarisation vector, so the imaginary part of the RMTF has to become as close to zero as possible. For that take the derivative of the imaginary part of the RMTF with respect to  $\phi$  and set it to 0.

$$\frac{\partial \text{Im} R(\phi)}{\partial \phi} \Big|_{\phi=0} = 0 \quad (3.10)$$

$$-K \frac{\partial}{\partial \phi} \int_{-\infty}^{+\infty} W(\lambda^2) \sin 2\phi (\lambda^2 - \lambda_0^2) d\lambda^2 \Big|_{\phi=0} = 0 \quad (3.11)$$

$$-K \int_{-\infty}^{+\infty} W(\lambda^2) 2(\lambda^2 - \lambda_0^2) \cos 2\phi d\lambda^2 \Big|_{\phi=0} = 0 \quad (3.12)$$

$$\int_{-\infty}^{+\infty} W(\lambda^2) (\lambda^2 - \lambda_0^2) d\lambda^2 = 0 \quad (3.13)$$

$$\lambda_0^2 = \frac{\int_{-\infty}^{+\infty} W(\lambda^2) \lambda^2 d\lambda^2}{\int_{-\infty}^{+\infty} W(\lambda^2) d\lambda^2} \quad (3.14)$$

where

$$K = \left( \int_{-\infty}^{+\infty} W(\lambda^2) d\lambda^2 \right)^{-1} \quad (3.15)$$

hence the constant  $\lambda_0^2$  should thus be equal to the weighted average of the observed  $\lambda^2$ .

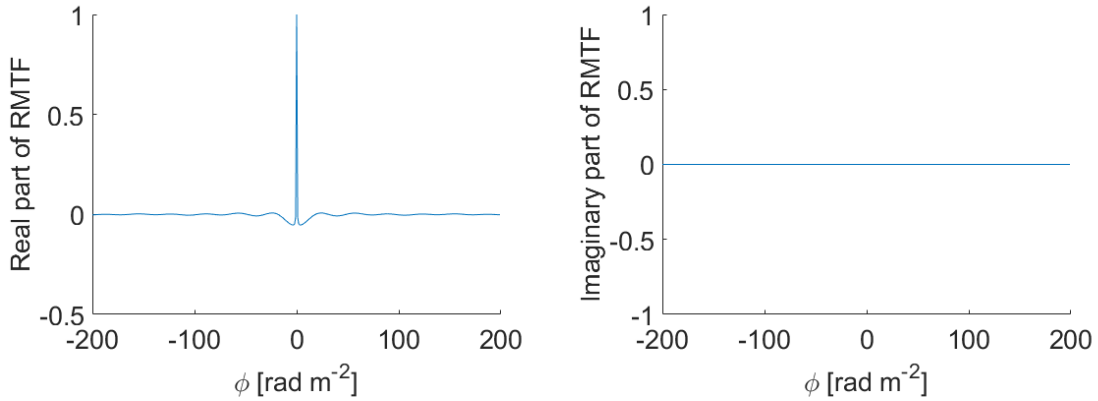


**Figure 3.3:** In the left panel: A narrow strong peak around  $\phi = 0$  and no visible oscillations around 0. In the right panel: The imaginary part of the RMTF for use in LOFAR is almost identical to 0 which is preferable. The used bandwidth was 120 MHz to 168MHz with a width of 1MHz for 480 channels (LOFAR HBA).

## 3.2 Experimental layout

There are limitations for what can be observed with this new approach. The rotation measure observation of polarised sources depends primarily on three parameters, the channel width, the width of the wavelength distribution squared,  $\lambda^2$  and the shortest wavelength squared,  $\lambda_{min}^2$ . They determine maximum observable Faraday depth, resolution in  $\phi$  space ( $d\phi$ ) and the size of the interval in  $\phi$  space. This can be seen from the eq. (3.19) where it is assumed the weight function is,

$$\begin{cases} 1, & \text{in } [\lambda_{min}^2, \lambda_{max}^2] \\ 0, & \text{anywhere else} \end{cases} \quad (3.16)$$

Theoretical limits for what is possible to detect with RM synthesis:

$$\delta\phi \approx \frac{2\sqrt{3}}{\Delta\lambda^2} \quad (3.17)$$

$$\Delta\phi_{max} \approx \frac{\pi}{\lambda_{min}^2} \quad (3.18)$$

$$|\phi_{max}| \approx \frac{\sqrt{3}}{\delta\lambda^2} \quad (3.19)$$

This means that when looking for small and faint polarised sources, it is important that the bandwidth of frequency (and consequentially the bandwidth of  $\lambda^2$ ) is as big as possible, so that the resolution in the Faraday space becomes as good as possible ( $\delta\phi$  is small).

For a fixed  $\phi$  - interval using the integral transformation from  $\lambda^2$  space to  $\phi$  space over a region in the sky one obtains a so-called *Faraday cube*. It is a cube with axes  $\alpha$  and  $\delta$  in the plane, where  $\alpha$  is right ascension and  $\delta$  represents declination and  $\phi$  in depth, see fig. 3.4. Studying one point in the sky for the coordinate  $(\alpha, \delta)$  yields a

### 3. The Faraday dispersion function

---

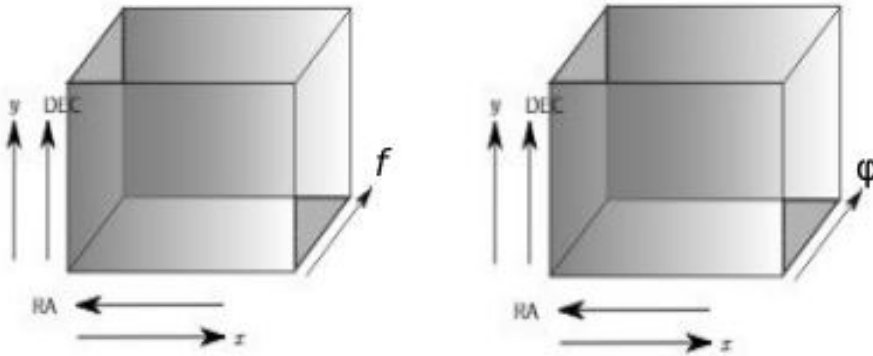


**Figure 3.4:** Left hand panel: A graphical presentation of a Frequency cube, consisting of an observed region of sky in multiple frequencies. Right hand panel: A graphical presentation of a Faraday cube. A Faraday cube is the transformed region, from  $f$  to  $\phi$  space.

Faraday spectrum  $F(\phi)$ . The application has allowed to discover very faint polarised emission [3].

In RM synthesis it is possible that a source is unresolved in  $\phi$  space, so that in  $\delta\phi$  is less than the width of the RMTF. Equation (3.5) shows that RMTF depends of the  $\lambda^2$  distribution. For an experimental layout the RMTF should therefore be known as accurately as possible. Main problems are frequency dependence of the primary beam attenuation, instrumental polarisation, synthesised beam size and the intrinsic emission spectra of the sources [3].

# 4

## Method for detection of polarised sources in LOFAR data

Although data from all stations (including international stations) were recorded, only data from the Dutch stations were used to produce the images of the public Data Release 2 (DR2 to occur in 2020) that are used in this work. For the purpose of detecting polarised sources automatically and efficiently, I have developed a script that can effectively handle the collected data. The data, file management and the script are described down below, the results are shown in chapter 5 and the main script can be found in the Appendix.

### 4.1 The LOFAR data

The LOFAR Two-metre Sky Survey (LoTSS) is a deep 120-168 MHz imaging survey that will cover the entire northern part of the sky. This is an ongoing survey which has a large potential for discoveries with applications in a wide range of research. The main scientific aims of the survey are to explore the formation and evolution of massive black holes, (e.g. Wilman et al. 2008 and Best et al. 2014) galaxies, clusters of galaxies (e.g. Cassano et al. 2010 and Brunetti & Jones 2014) and large-scale structure (Shimwell et al. 2019). The earliest data release was the preliminary data release (PDR), which consists of 350 square degrees in the region of the HETDEX Spring field <sup>1</sup> imaged at a resolution of 25 arcsec and an averaged noise level less than 0.5 mJy/beam. Over 35000 sources were detected and is described in the article Shimwell et al. 2017. Data release 1 (DR1) consists of images at the full resolution (6 arcsec) and sensitivity (better than 0.1 mJy/beam) of Dutch LOFAR over 400 square degrees in the region of the HETDEX Spring field. Over 325 000 sources were detected. The data release includes optical counterparts for 71% of the radio sources (Williams et al. 2019) and photometric redshifts for these sources (Duncan et al. 2019). DR1 is described in the article Shimwell et al. 2019.

The Dutch stations have for the new data release DR2 observed in the northern sky for which I have used the data to work with. DR2 is so far available only for the members of the LOFAR Surveys and of the MKSP teams for which I have been invited to work with and preparations for a second data release is under way. The aim to release images and catalogues for 2500 square degrees of the northern sky by 2020. The regions of the sky are categorised in regions called *Hetdex*. They are in turn divided into smaller regions called *pointings*. 3168 pointings are required to cover the entire

---

<sup>1</sup>right ascension  $10^h45^m00^s$  to  $15^h30^m00^s$  and declination  $45^\circ00'00''$  to  $57^\circ00'00''$

northern sky. I have studied a pointing from the DR2 data named P39Hetdex19 which covers an area of the sky that contains the nearby galaxy M51, see fig. 4.1.

The images are stored in so-called FITS-files (*Flexible Image Transport System*). FITS-files are often used in astronomy for digital storage, in transmission and processing of data) which can be manipulated on computers. The FITS files I have used contains LoTSS images of all Stokes parameters ( $I$ ,  $Q$ ,  $U$  and  $V$ ) in different frequency channels.

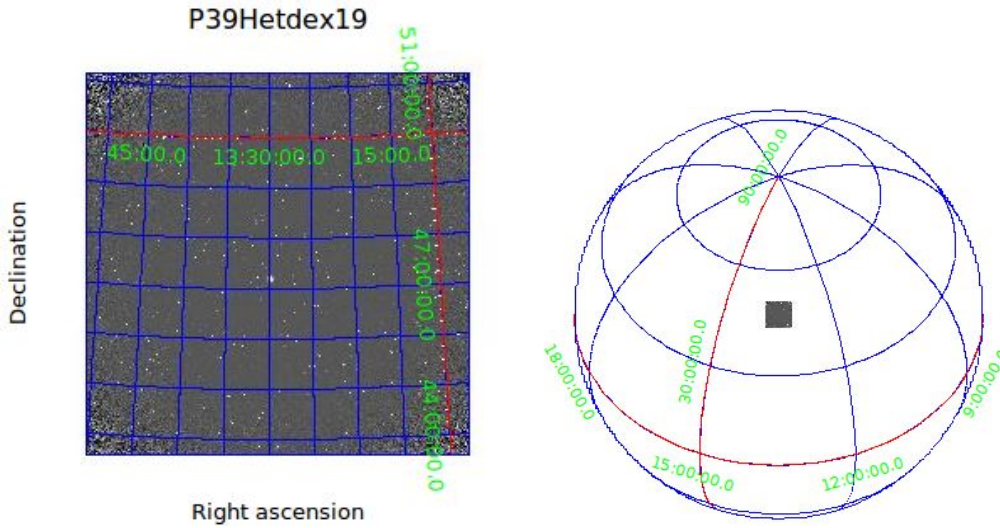


**Figure 4.1:** Left panel: Stokes I image of pointing P39Hetdex19 with galaxy in the centre. Right panel: Location of the pointing on the celestial sphere ( $RA \approx 13h\ 30m$ ,  $DEC \approx 47^\circ$ ).

## 4.2 Preparation before running the algorithm

I had to my disposal a search engine into LOFAR's data survey to download the FITS-files from LOFAR's DR2 base and for this report I downloaded files which had a resolution of 20 arcseconds. The download could be performed by entering known sources, such as M51, which would appear in the centre of the file or I could type in  $RA-DEC$  coordinates and then decide which radius I wanted, which determined the size of the files. Older observational data files and where future release will be uploaded can be found on LOFAR's survey's website <sup>2</sup>.

### 4.2.1 Selecting specific regions in space and constructing Faraday cubes

In some cases there were small interesting regions of the sky, worth to investigate and in those cases one could benefit from copying out smaller regions from one pointing instead of downloading an entire image centred around those regions from the DR2 base, which saved much time. This was done with command "fitscopy". The correct

<sup>2</sup><https://www.lofar-surveys.org/>



syntax for copying looks in Unix like:

**fitscopy LargeFile.fits [a:b, c:d] NewSmallFile.fits**, where the copying is done from pixel  $a$  to  $b$  in positive  $x$  direction and  $c$  to  $d$  in positive  $y$  direction from the large file (for instance a pointing) named here *LargeFile.fits* to the smaller file named here *NewSmallFile.fits* and it worked equally well for any FITS file, including Faraday cubes. This turned out to be extremely useful when studying many sources scattered over one large area.

### 4.2.2 Constructing Faraday cubes

Faraday transformation on the images is performed with *pyrmsynth* or *pyrmsynth\_lite* files in assistance of a key parameter file *rmsynth* which set parameter values for the Faraday cube. The code which was developed by a team member of MKSP can be partly found here <sup>3</sup> and here <sup>4</sup> which is constantly updated. Before performing Faraday transformation, the intensity image was "masked" in order to evaluate Faraday spectra only over "bright sources". The flux density threshold was specified by recommendation to be at 1 mJy. Using a mask file, the pixels with values below 1 mJy were replaced by "NaNs" (Not a number) and pixels above that threshold were replaced by 1 in the intensity file. The value in this process lies to reduce noise and time.

## 4.3 Description of the algorithm

The user wanting to find polarised sources using this algorithm, must provide the (masked) intensity file and the corresponding Faraday cube. The code will automatically print out coordinates for all polarised sources over the examined region.

### 4.3.1 Reading the data

In this work I used the Matlab software. The Faraday cube file is inserted in a three dimensional array. One can visualise the three dimensional array as a "3D matrix", with the  $x$  and  $y$  - axes as one plane/slice representing the entire region in the  $\phi$  - space. The intensity map is inserted in to a two dimensional array, a regular matrix, with the  $x$  and  $y$  - axes representing the region. The FITS files are opened in Matlab using the commando *fitsopen*.

### 4.3.2 Detection of radio continuum sources on the intensity map

In this step the code locates radio continuum sources in the region by filtering the two dimensional array to a binary matrix and then identifies the sources. If the intensity map has been masked before, this part of the script will not change significantly the two dimensional array. The adjustment of the values in the two dimensional array is performed in Matlab using the command "imadjust", which changes contrast and

---

<sup>3</sup><https://github.com/sabourke>

<sup>4</sup><https://github.com/mrbell/pyrmsynth>

brightness in the matrix. There are several parameters and options for how to conduct this and change the image, which can be found on Matlab's own website<sup>5</sup>. Identifications and locating groups of neighbouring pixels as blobs is done with the commands "find"<sup>6</sup>, "bwconncomp"<sup>7</sup> and "regionprops"<sup>8</sup>. All the commands together in this step of the algorithm, finds and identifies neighbouring non-zero elements constituting as "islands" or "blobs" (and also find the blobs' centroids), which in the intensity map are radio continuum sources.

### 4.3.3 Identifying polarised sources and Faraday spectra

In the last step the algorithm evaluates Faraday spectra for all radio continuum sources and checks whether the Faraday spectra passes a specific threshold condition while ignoring the instrumental polarisation. In order for a radio continuum source to very likely be categorised as a polarised source, its Faraday spectrum  $F(\phi)$  needs to fulfil the condition that the  $S/N$  ratio is larger than 6 and to take into account instrumental polarisation the  $\phi$  value for the signal cannot be inside a small interval close to 0. All Faraday spectra are individual and it cannot be told in beforehand how large the  $\phi$  interval should be considered to be a part of instrumental polarisation. From experience and through recommendation, I excluded the interval of Faraday depths  $\phi \in [-3, 1]$  rad/m<sup>2</sup> that might be contaminated with instrumental polarisation. To compute the standard deviation  $\sigma$ , and mean of the spectra  $\mu$ , there are simple commands in Matlab. The commands are applied in the interval everywhere but in  $\phi \in [-3, 1]$  so  $\sigma$  and  $\mu$  are also computed outside this interval.

#### 4.3.3.1 Reproduced Faraday spectrum with a specific resolution

Changing the resolution could change significantly the values in  $F(\phi)$ , it sometimes shifted crucial peaks to other  $\phi$  values or sometimes they even disappeared. The code is applied for one pixel per run, resulting the code works at a much smaller resolution than the observational data since one pixel corresponds to 0.00125 degrees or 4.5 arcseconds in diameter. To best find polarised sources in Matlab, one must work with the same resolution as the processed files. The FITS files used for this report have a resolution of 20 arcseconds in diameter, which corresponds to about 16 pixels or in other words about a  $4 \times 4$  grid of pixels. This means to obtain the Faraday spectrum for "one position" equals to average the Faraday spectra in a  $4 \times 4$  grid of pixels around the position. This process can be compared to a sort of filtering. This is performed with a convolution and I used convolution the commando conv2<sup>9</sup>. Despite there are many efficient ways, it was the fastest way which paid off for big data sets. Having taking into account resolution, the code produces more accurately Faraday spectra and writes all polarised sources' image coordinates and  $\phi$  - values in to a new text-file. The user may want to open and visualise these radio continuum sources' coordinates in ds9. In ds9 the degree and  $RA - DEC$  coordinates can be extracted.

---

<sup>5</sup><https://se.mathworks.com/help/images/ref/imadjust.html>

<sup>6</sup><https://se.mathworks.com/help/matlab/ref/find.html>

<sup>7</sup><https://se.mathworks.com/help/images/ref/bwconncomp.html>

<sup>8</sup><https://se.mathworks.com/help/images/ref/regionprops.html>

<sup>9</sup><https://se.mathworks.com/help/matlab/ref/conv2.html>

In the code I have added the option to plot the location of all found polarised sources in the intensity map.



# 5

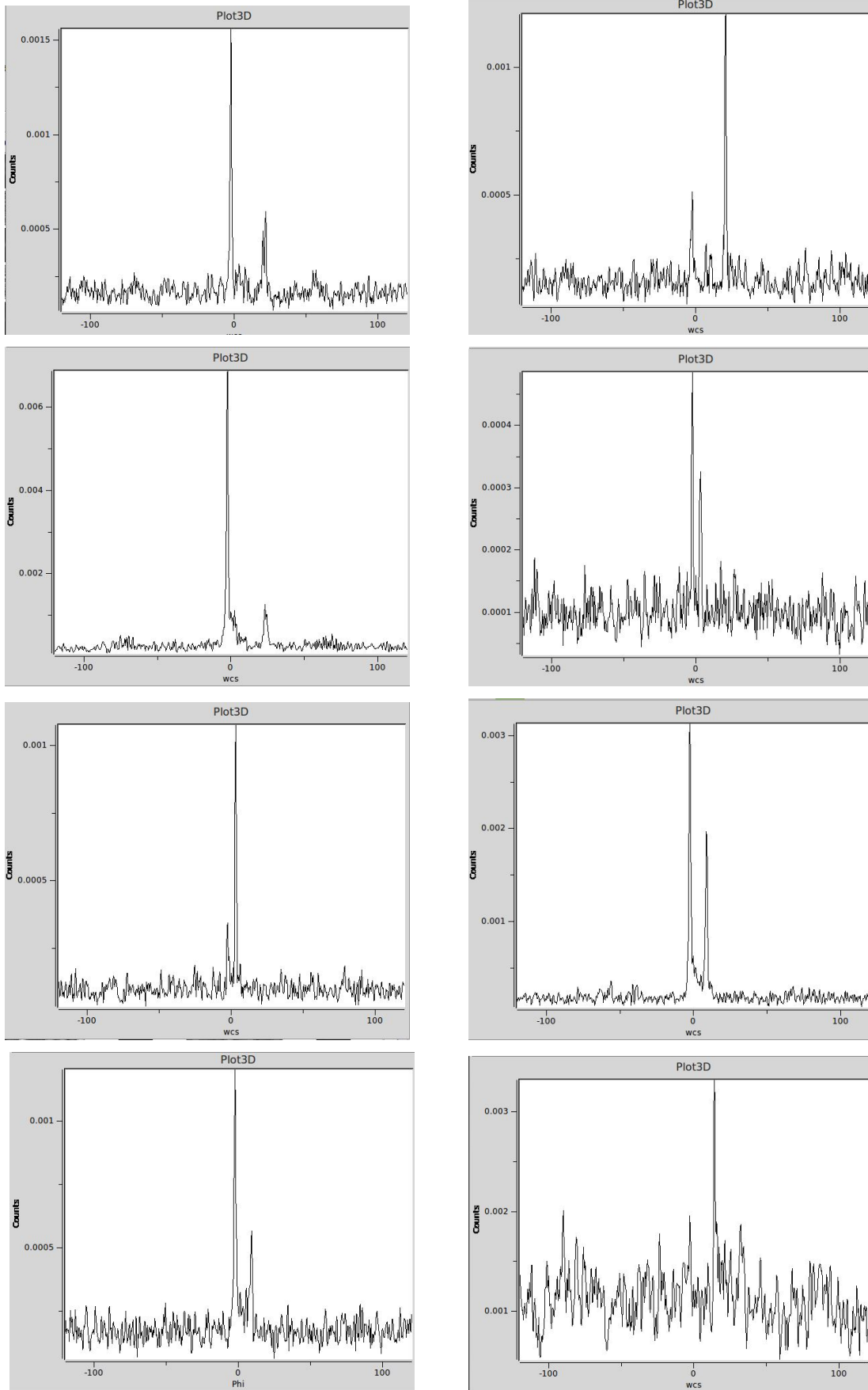
## Results

I used the algorithm presented in chapter 4 to search for polarised sources in the LoTSS pointing P39Hetdex19 of the LOFAR data release 2 (DR2). First I applied the algorithm to the regions in which polarised sources were identified in an analysis of earlier LOFAR observations of the field (Neld et al. (2018)).

### 5.1 Comparison with the Neld et al. (2018) analysis

In the article Neld et al. (2018) co-authored by several members of MKSP [19], published they have found 19 new potential polarised sources in the article using DR1. The top 6 most likely polarised sources had a 5% risk to be false detections while the other (13) were expected to have 50% false detections. The team have worked on calibrated, pointed LOFAR measurements of the M51 field, which was observed in 2013 for eight hours with HBA. I checked if my script could detect the sources as polarised sources using DR2. In the article they published the coordinates of the radio-continuum sources. The results from my script showed that 11 out of 19 radio-continuum sources from the paper Neld et al. (2018) have at least one polarised source. The results are shown in form of Faraday spectra, downloaded from ds9.

## 5. Results



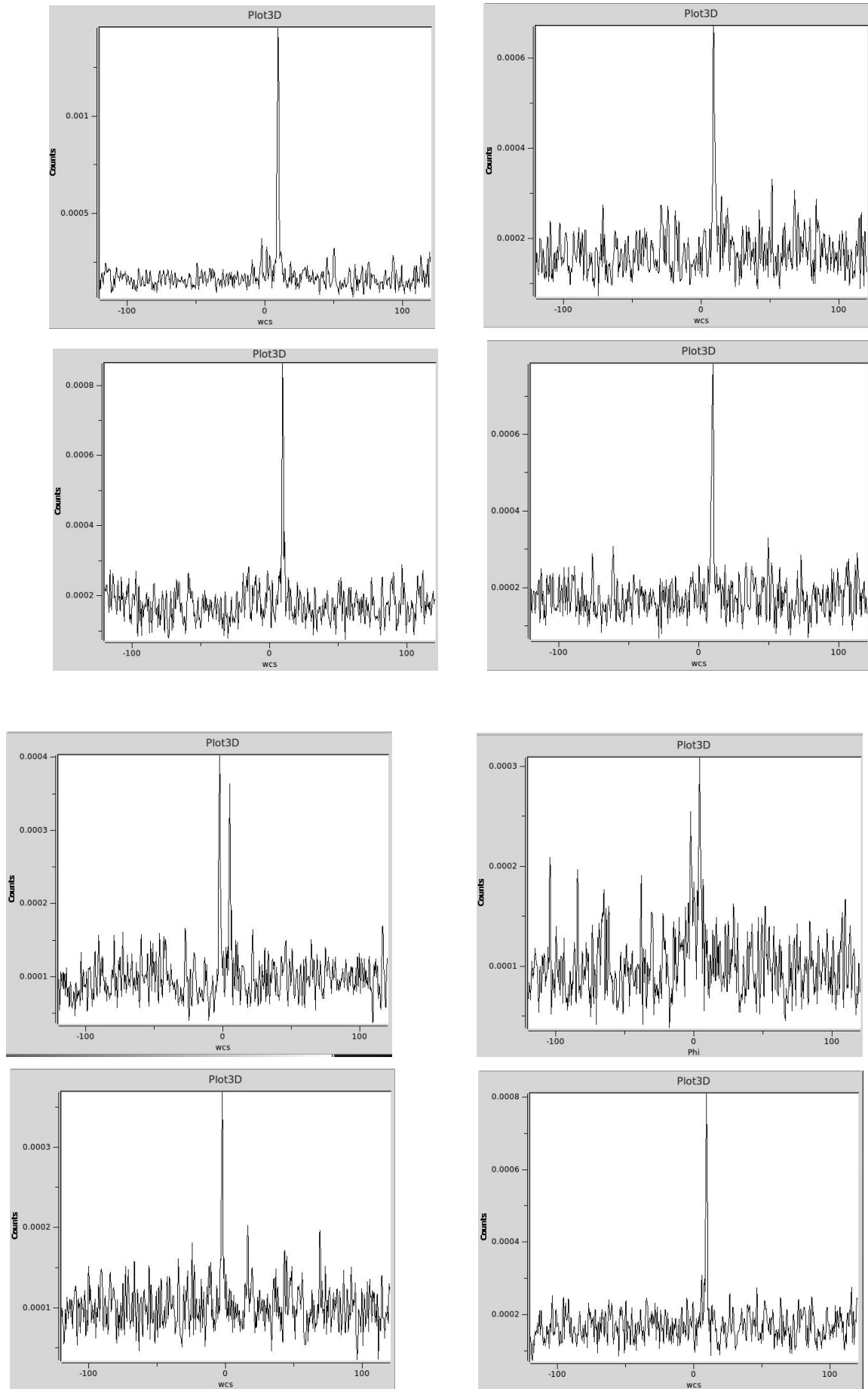


**Figure 5.1:** Faraday spectra for all identified polarised components and sources.

## 5. Results

#	RA(J2000)	Dec(J2000)	$\phi_{Neld}$	$\phi_{ds9}$	$\phi_{code}$ (in its close surrounding)
1a	13 <sup>h</sup> 39 <sup>m</sup> 23 <sup>s</sup>	+46°40'18"	20.4 ± 0.1	20,21.75	21.9,22.2
1b	13 <sup>h</sup> 39 <sup>m</sup> 19.994 <sup>s</sup>	+46°41'13.68"	20.4 ± 0.1	20.6	20.4,20.7,21
2	13 <sup>h</sup> 41 <sup>m</sup> 45 <sup>s</sup>	+46°57'19"	23.2 ± 0.1	23	23.1,23.4
3a	13 <sup>h</sup> 26 <sup>m</sup> 33.560 <sup>s</sup>	+47°37'42.88"	3.0 ± 0.1	3	3.3
3b	13 <sup>h</sup> 26 <sup>m</sup> 29.557 <sup>s</sup>	+47°37'38.06"	3.0 ± 0.1	3	2.7,3,3.3,3.6,3.9
4a	13 <sup>h</sup> 37 <sup>m</sup> 08 <sup>s</sup>	+48°58'3"	9.0 ± 0.1	9	8.7,9,9.3,9.6
4b	13 <sup>h</sup> 37 <sup>m</sup> 06.720 <sup>s</sup>	+48°57'47.20"	9.0 ± 0.1	9	9.3,9.6
5	13 <sup>h</sup> 32 <sup>m</sup> 45.798 <sup>s</sup>	+44°53'29.74"	14.0 ± 0.1	14	14.4,14.7
6a	13 <sup>h</sup> 36 <sup>m</sup> 17.330 <sup>s</sup>	+49°00'50.32"	9.2 ± 0.1	9.4	9.3,9.6
6b	13 <sup>h</sup> 36 <sup>m</sup> 12.245 <sup>s</sup>	+49°00'28.97"	9.2 ± 0.1	8.8	9.3,9.6
6c	13 <sup>h</sup> 36 <sup>m</sup> 19.421 <sup>s</sup>	+48°59'28.79"	9.2 ± 0.1	8.8	9.3,9.6
6d	13 <sup>h</sup> 36 <sup>m</sup> 14.543 <sup>s</sup>	+49°00'32.95"	9.2 ± 0.1	10	9.6,9.9
8	13 <sup>h</sup> 30 <sup>m</sup> 52 <sup>s</sup>	+47°59'31"	57.8 ± 0.1	5	5.1,5.4
12	13 <sup>h</sup> 29 <sup>m</sup> 11.228 <sup>s</sup>	+48°3'54.81"	-5.0 ± 0.1	4	4.2,4.5
15	13 <sup>h</sup> 32 <sup>m</sup> 57.201 <sup>s</sup>	+47°0'48.53"	16.6 ± 0.1	16.3	16.5
18	13 <sup>h</sup> 37 <sup>m</sup> 38 <sup>s</sup>	+49°04'42"	8.8 ± 0.1	9	8.7,9,9.3,9.6,9.9

**Table 5.1:** The results from the code applied with the condition  $S/N > 6$ . We notice that almost all of the radio continuum sources that have been found to have at least one polarised component have the same Faraday depth as in the referred article, except for source 8 and source 12. Source 8 has a considerable change. The letters in front some of the sources indicate there is more than one polarised component.

### 5.2 Region 2

Region 2 is a part of P39Hetdex19 centred around M51 galaxy, see fig. 5.2 (right ascension 13<sup>h</sup>22<sup>m</sup>25<sup>s</sup> to 13<sup>h</sup>33<sup>m</sup>00<sup>s</sup> and declination 46°29'00" to 47°32'00").

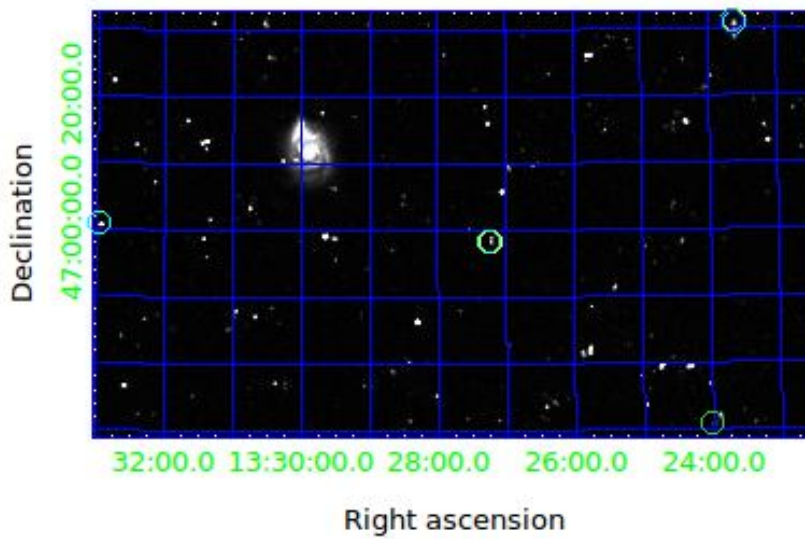


**Figure 5.2:** The large galaxy is the M51 galaxy. The circles represent polarised sources found by the algorithm.



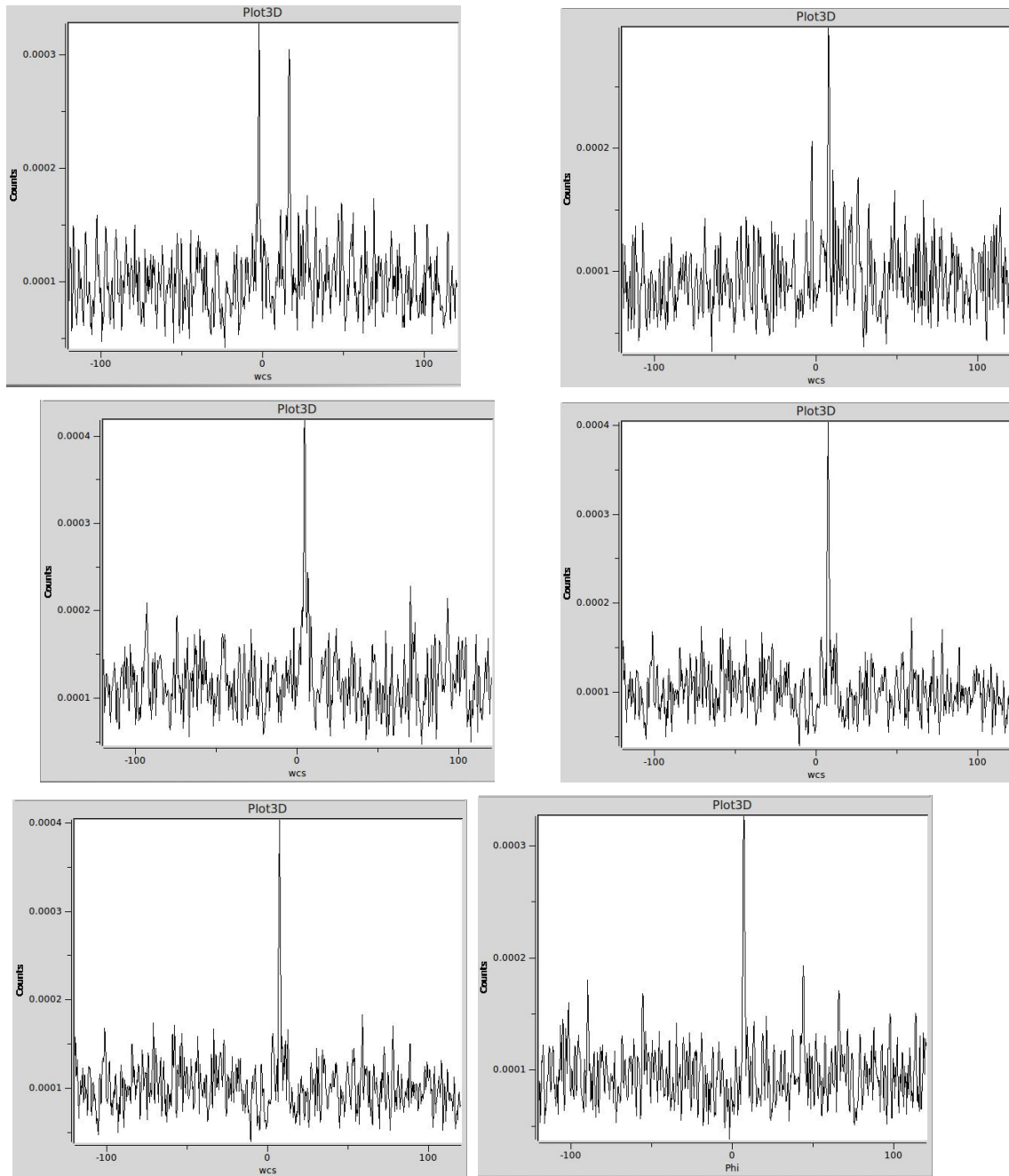


**Figure 5.3:** Faraday spectra for all identified polarised components and sources.

## 5. Results

RA(J2000)	Dec(J2000)	$\phi_{ds9}$ [rad/m <sup>2</sup> ]	$\phi_{code}$ [rad/m <sup>2</sup> ] (in its close surrounding)
13 <sup>h</sup> 32 <sup>m</sup> 57.201 <sup>s</sup>	+47°00'48.53"	16.3	16.5
13 <sup>h</sup> 27 <sup>m</sup> 13.199 <sup>s</sup>	+46°58'14.07"	7.5	7.8, 8.1
13 <sup>h</sup> 23 <sup>m</sup> 59.666 <sup>s</sup>	+46°30'47.45"	4.5	4.5, 4.8
13 <sup>h</sup> 23 <sup>m</sup> 59.666 <sup>s</sup>	+46°30'47.45"	7.3	7.5, 7.8
13 <sup>h</sup> 23 <sup>m</sup> 36.212 <sup>s</sup>	+47°30'35.09"	6.9	6.9, 7.2, 7.5
13 <sup>h</sup> 23 <sup>m</sup> 35.729 <sup>s</sup>	+47°30'57.51"	7	6.9, 7.2

**Table 5.2:** The results presented in the tabular are findings from the code applied with  $S/N > 6$ .

### 5.3 Subfield near source 6 from the article Neld et al. (2018)

This region (right ascension 13<sup>h</sup>35<sup>m</sup>10<sup>s</sup> to 13<sup>h</sup>38<sup>m</sup>33<sup>s</sup> and declination 48°42'30" to 49°29'00" ) contains many what can be polarised sources in a relatively small region. It is also interesting to study a bit closer source 6 from article [19] since it has many polarised components.

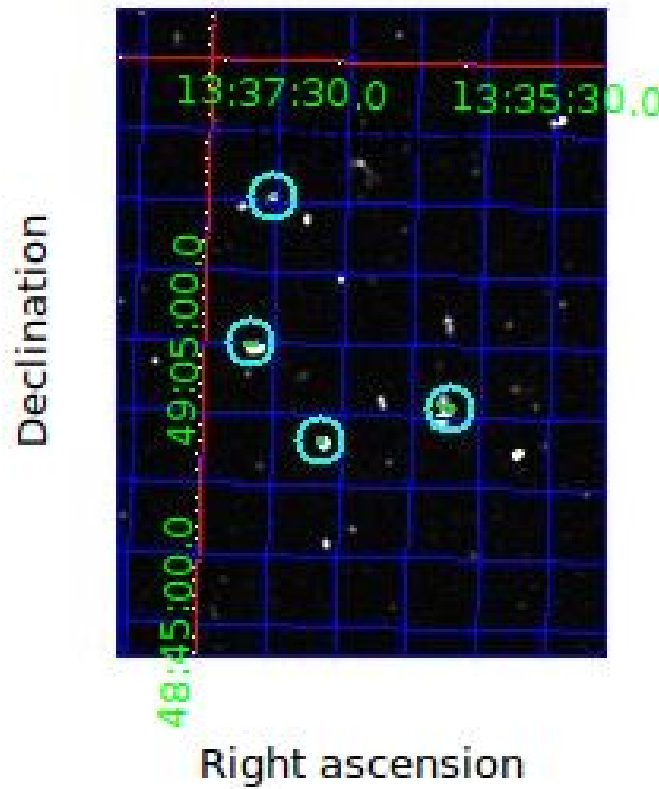


**Figure 5.4:** A list of the coordinates from all sources are to be found at the end of the section. The location of source 6 is encircled by the bottom right circle.

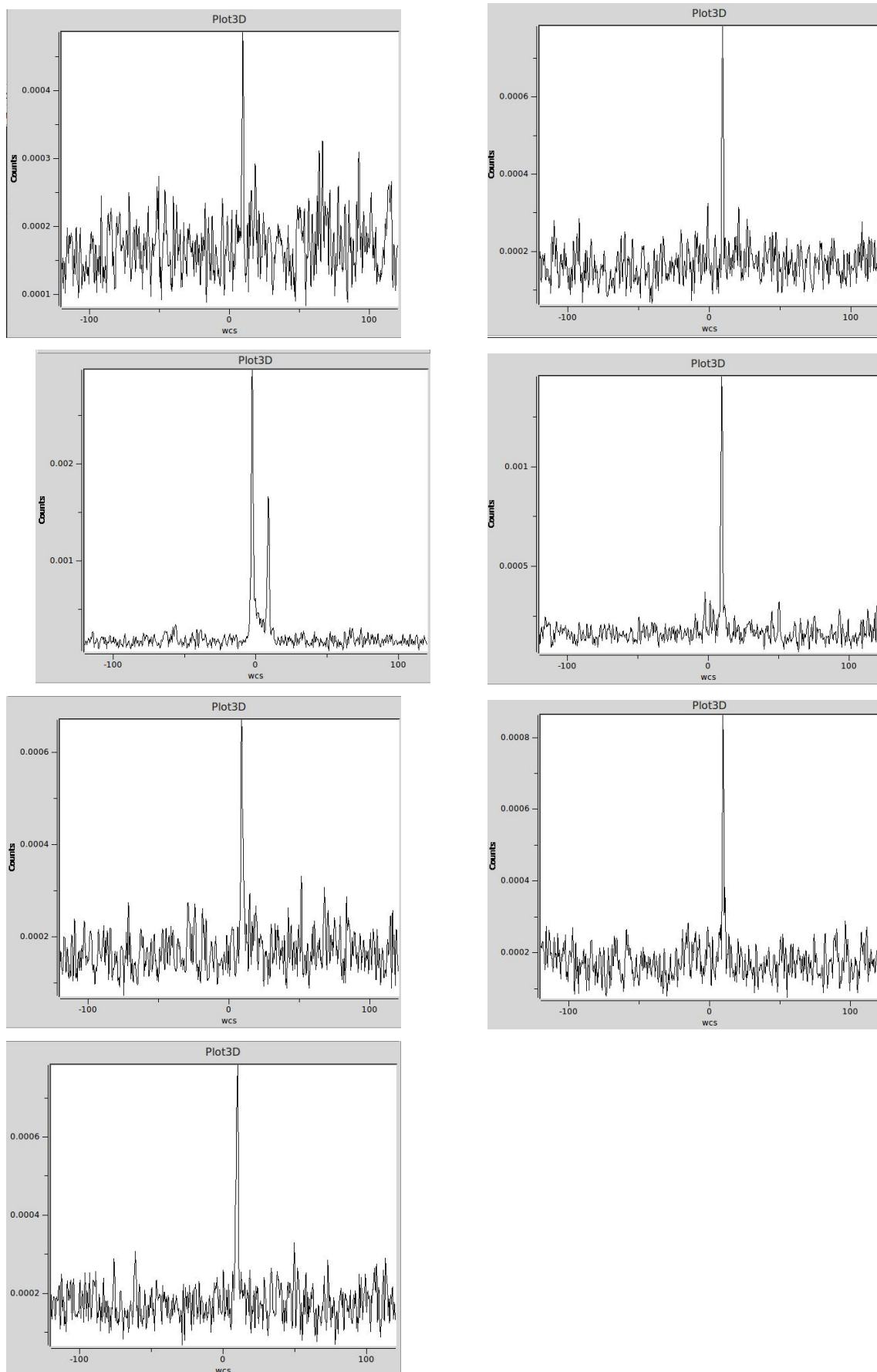


**Figure 5.5:** Faraday spectra for all identified polarised components and sources.

## 5. Results

RA(J2000)	Dec(J2000)	$\phi_{ds9}$ [rad/m <sup>2</sup> ]	$\phi_{code}$ [rad/m <sup>2</sup> ] (in its close surrounding)
13 <sup>h</sup> 37 <sup>m</sup> 30.089 <sup>s</sup>	+49°15'21.36"	9.3	9.3,9.6
13 <sup>h</sup> 37 <sup>m</sup> 39.456 <sup>s</sup>	+49°4'37.34"	9.3	9.3,9.6
13 <sup>h</sup> 37 <sup>m</sup> 08.126 <sup>s</sup>	+48°58'0.35"	9	9.3,9.6
13 <sup>h</sup> 36 <sup>m</sup> 17.330 <sup>s</sup>	+49°00'50.32"	9.4	9.3,9.6
13 <sup>h</sup> 36 <sup>m</sup> 12.245 <sup>s</sup>	+49°00'28.97"	8.8	9.3,9.6
13 <sup>h</sup> 36 <sup>m</sup> 19.421 <sup>s</sup>	+48°59'28.79"	8.8	9.3,9.6
13 <sup>h</sup> 36 <sup>m</sup> 14.543 <sup>s</sup>	+49°00'32.95"	10	9.6,9.9

**Table 5.3:** The results presented in the tabular are findings from the code applied with  $S/N > 6$ .

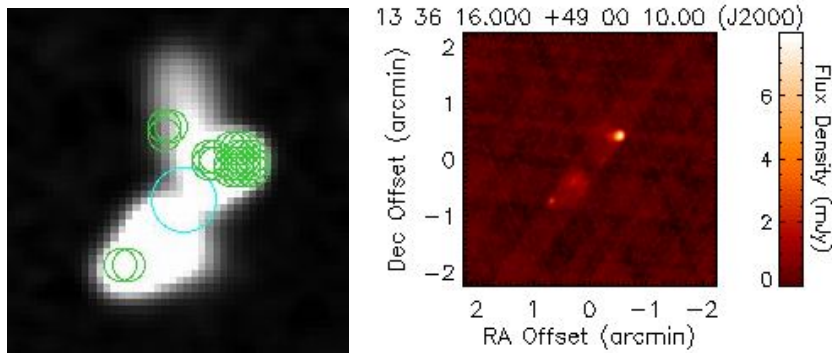


**Figure 5.6:** Source 6 shown in the intensity map observed by LOFAR and FIRST. The cyan coloured circle represents the location of the coordinate for source 6 found in the article [19], the green circles show the location of the identified polarised sources. Left panel: Intensity map observed at 150 MHz with 20'' resolution, dimensions of the image is (right ascension 13<sup>h</sup>36<sup>m</sup>06<sup>s</sup> to 13<sup>h</sup>36<sup>m</sup>27<sup>s</sup> and declination 48°58'31" to 49°02'15") Right panel: Intensity map observed with FIRST at 1.4 GHz with 5'' resolution.

# 6

## Outlook

The following section will provide some discussion on the results, method and give a brief outlook.

### 6.1 Discussion of results

The application of the code has revealed some new polarised sources and many of them have more than one component of radio polarisation. The main source of radio polarisation in jets is synchrotron emission and what one expects is therefore one or two polarised sources / polarised components per radio continuum galaxy however some radio continuum sources appeared to have three and an extreme case is source 6 from article [19] which has 4 polarised components. The code has worked in excellent agreement with the ds9 software

#### 6.1.1 Many polarised sources

The code applied to polarised sources shows many times many polarised components. It happens that they are often located very close to each other for a polarised sources which cannot be easily distinguished. Physically it can be interpreted as they are originating from one polarised source in the radio galaxy, and the polarised source is probably a large magnetic field structure in the radio galaxy. The several  $\Phi$  values found under the column  $\phi_{code}$  for a specific radio galaxy hints of different magnitude, shape and direction of the magnetic field acted on the jets. This results in that the script prints the same and similar coordinates more than one time which is shown in the intensity map. The shape for this radio galaxy is irregular and it is possible that the magnetic field around the jets is tangled and strong enough to bend the jets, on both lobes and as such have additional polarised components on both sides, see fig. 5.6.

### 6.2 The code

During the preparation of the FITS files that have been used for work, the intensity map was masked in order to save computer time when performing the Faraday cube. This means that all pixels below the threshold value are not taken in to account in the production of the Faraday cube. This constraints a limit on the number of pixels that can be analysed later. I have given instructions in my script to adjust and filter

the two dimensional array which is also a masking process, and which removes some pixels to also save computer time. Consequently my script can only detect as many polarised sources as before the masking in the preparation process or less, since the Faraday cube is affected by it. One might seem to think that it might be unnecessary to mask, however the reason is it would save time in case the user would have access just to the intensity map and the Faraday cube, which can be found on the LOFAR surveys web page and not have access to the the masked intensity map. In case the user have access to the masked intensity map he/she could still work with the script since Matlab requires a binary matrix for the next steps.

### 6.3 The algorithms consistency with the ds9

Whenever my code found an indication in a Faraday spectrum corresponding to a polarised source, this was always confirmed by visual inspection using the ds9 software. This is a very promising start for the script in future use. Despite taking into account some factors in the script such as resolution, the Faraday spectrum could differ a little bit.

The ds9 software have no problems working with pixels which have coordinates at non-integer values. For example a position of (24.895, 25.123) and ds9 could produce a Faraday spectrum for exactly this position whereas in Matlab it is not possible to work on this position. In my script I would need to examine (25, 25). On small scales this has importance for the resolution and it could be worth investigating.

### 6.4 Conclusions and outlook

The initial goal was to automate the process of detection of polarised sources: to develop a code that detects polarised sources in a specific region of the sky. This can be more precisely described as detecting outliers in a multidimensional array (3D cube) representing the polarised sources. An algorithm has been developed and the script has consistently worked well with a well established software used extensively by astronomers and by using new data release DR2, the code has produced new results. In conclusion this goal has been achieved. Despite that it works well there is still room for improvement. One of my main issues in this report was the limitation of the memory space on the hardware and software I worked on (RAM space), while the time complexity could have been improved. While the investigated areas are interesting they are however very small compared to P39Hetdex19 which in turn is a small part of the sky, which inhibited the progress of discovering larger parts of the sky. Due to the enormous sizes of the files, especially the Faraday cubes, I abstained from working with a higher resolution in  $\phi$  space in those regions. An improvement of the algorithm with commando *Isoutlier*<sup>1</sup> in Matlab would have increased the algorithm's efficiency yet it is limited to detect outliers with  $S/N > 3$ . In data science there is a whole research field devoted for developing algorithms which can efficiently detect outliers in multidimensional arrays, and it is obvious that Big data analysis has

---

<sup>1</sup><https://se.mathworks.com/help/matlab/ref/isoutlier.html>

become important in astrophysics, there are developed algorithms for detecting outliers presented in research papers [6]. In the future it will be necessary to have more powerful hardware and implement smarter algorithms that will cope with the large data amounts.





# Bibliography

- [1] ASTRON Netherlands Institute for Radio Astronomy, *Lofar stations: Description and Layout*  
URL: <http://old.astron.nl/radio-observatory/astronomers/users/technical-information/lofar-stations/lofar-stations-description->
- [2] Best, P. N., Ker, L. M., Simpson, C., Rigby, E. E., & Sabater, J. 2014, MNRAS, 445, 955
- [3] Brentjens M.A & de Bruyn A.G., A&A, 441, 1217-1228 (2005) (*Faraday rotation measure synthesis*)
- [4] Brunetti, G., & Jones, T. W. 2014, Int. J. Mod. Phys. D, 23, 1430007
- [5] Cassano, R., Brunetti, G., Röttgering, H. J. A., & Brüggen, M. 2010, A&A, 509, A68
- [6] Charu C. Aggarwal & Philip S. Yu, ACM SIGMOD Record, Volume 30 Issue 2, Pages 37-46 (June 2001) (*Outlier Detection for High Dimensional Data*)
- [7] Chris Flynn, Tuorla observatory *Accretion disks* (URL:<http://www.astro.utu.fi/~cflynn/astroII/16.html>)
- [8] Condon James J. & Ransom Scott M., Princeton University press (2016) *Essential Radio Astronomy*
- [9] Duncan, K., Sabater, J., Rottgering, H., et al. 2019, A&A, 622, A3 (LOFAR SI)
- [10] Eline Tolstoy, Kapteyn Astronomical Institute *Radiative Processes in Astrophysics*  
URL:<https://www.astro.rug.nl/~etolstoy/astroa07/lecture9p.pdf>
- [11] Frank H. Shu, *Radio jet* URL:<https://www.britannica.com/science/radio-jet>
- [12] John C. Bancroft, *Introduction to matched filters*, CREWES Research Report, Volume 14 (2002)  
(URL:<https://www.crewes.org/ForOurSponsors/ResearchReports/2002/2002-30.pdf>)
- [13] LOFAR, *The science drivers of LOFAR - the Key Science Projects (KSP)*,  
URL:<http://www.lofar.org/astronomy/key-science/lofar-key-science-projects>
- [14] LOFAR, *Cosmic Magnetism* URL:<http://www.lofar.org/astronomy/cosmic-magnetism/cosmic-magnetism>
- [15] LOFAR Surveys website URL: <https://www.lofar-surveys.org/>
- [16] Mehlig, B., University of Gothenburg, Department of Physics, *Lecture notes Artificial Neural Networks* (2018)
- [17] Moo K. Chung, University Ave, Madison (Teaching)  
(URL:<http://pages.stat.wisc.edu/mchung/teaching/MIA/reading/diffusion.gaussian.kernel.pdf.pdf>)

- [18] National Radio Astronomy Observatory *Magnetobremssstrahlung* URL: <https://www.cv.nrao.edu/course/ast534/Magnetobremssstrahlung.html>
- [19] Neld A., Horellou C., Mulcahy D.D et al., A&A 617, A136 (2018) (*Reliable detection and characterization of low frequency polarized sources in the LOFAR M51 field.*)
- [20] Onsala Space Observatory, SKA - SwedishScienceCase2015 URL:<http://www.chalmers.se/en/researchinfrastructure/oso/radio-astronomy/ska/Documents/SKA-SwedishScienceCase2015.pdf>
- [21] Shimwell et al., A&A, 598, A104 (2017) (*The LOFAR Two-metre Sky Survey – I. Survey Description and Preliminary Data Release*)
- [22] Shimwell et al., A&A, 622, A1 (2019) (*The LOFAR Two-metre Sky Survey – II. First data release*)
- [23] Sparke L.S. & Gallagher J.S., Cambridge University press (2012), *Galaxies in the Universe: An introduction second edition* p. 366-383
- [24] van Harleem M.P et al., A&A 556, A2 (2013) *Lofar: The LOw-Frequency ARray*
- [25] Williams, W. L., Hardcastle, H. J., Best, P. N., et al. 2019, A&A, 622, A2 (LOFAR SI)
- [26] Wilman, R. J., Miller, L., Jarvis, M. J., et al. 2008, MNRAS, 388, 1335 *A semi-empirical simulation of the extragalactic radio continuum sky for next generation radio telescopes*
- [27] (image) LOFAR Users Meeting R. F. Pizzo Head Science Operations & Support (image) Seminar 20 - 23 May, Leiden Netherlands  
URL: [https://www.astron.nl/lofarscience2019/Documents/Monday/LUM\\_Pizzo.pdf](https://www.astron.nl/lofarscience2019/Documents/Monday/LUM_Pizzo.pdf)
- [28] (image), Sky&Telescope  
URL:<http://www.ita.uni-heidelberg.de/~vgaibler/agnjets.html>
- [29] (image) Subramanian Kandaswamy, *Galactic Magnetic Fields*, Nordita class 2017  
URL:<https://www.nordita.org/docs/agenda/slides-masterclass2017-subramanian-1.pdf>
- [30] (image) Towards data science *Training Deep Neural Networks Deep Learning Accessories*  
URL:<https://towardsdatascience.com/training-deep-neural-networks-9fdb1964b964>

# Appendix

## The Algorithm

### Machine learning algorithm - a different approach of detecting polarised sources

I have tried a different approach using a machine learning algorithm as an attempt to detect what can be polarised sources from Faraday spectrum. Larger data set are inevitable and using machine learning should be a familiar tool for astronomers and astrophysicists in the future on daily basis. This is to my knowledge the first attempt to apply machine learning to radio polarisation data. In this approach I used Matlab which has its own convenient Machine learning tool. Matlab's own Machine learning tool simplifies the work, since any manipulations in the network such as changing number of neurons or hidden layers does not require any intervention. Because of its flexibility it is very simple to add or remove neurons and layers and test the networks' performance in a short time span. The standard network consisted of one hidden layer with 20 neurons and one output layer called a *Softmax layer*, that gives out ones and zeros.

### Theory behind the use of neural network

The idea behind teaching the network was based on *supervised learning* and the *classification task*. Supervised learning means that all relevant input data will be assigned to output values. In general it is described as a function that maps an input value to an output value based on example input-output pairs, while a classification task imply the network will work on correctly classifying the input-output pairs from that function. One usually visualises this as a mapping from vectors in a  $N$  dimensional space to a vector in  $M$  dimensional space. To understand the underlying theory of how neural networks work, we must define some objects. It is important to be able to visualise a structure of a network and see how connections can flow between neurons in layers. One can visualise the small network as a simple model for how the brain works. We start with representing a network with vectors and matrices. The vector  $\mathbf{x}^\mu = [x_1, x_2, \dots, x_N]$  is a vector consisting of  $N$  components or neurons and the  $\mu$ th *pattern*. This vector is called an *input vector* which is put in to the network. The objective of the network is to pair a pattern with the correct target. The strength of the connection from neuron  $i$  in one layer to neuron  $j$  in the next layer is denoted by  $w_{ij}$ . This is the *weight matrix* which transforms the vector in layer  $k$  from  $N$  space to the

$P$  space in layer  $l$ . This matrix contains information about "strength" between the links of neurons. As in the brain, in order for the neurons to fire (be active), they need to pass a certain threshold  $\theta_i$ , to send out a signal. This has also been adopted for artificial networks. To update the neuron one must have a so-called *activation function*  $g$ . This have as an argument the product of the weight matrix and the vector, where sometimes is the threshold included all summarised in  $b$ ,

$$\begin{cases} b_i^\mu = \sum_{j=1}^N w_{ij} x_j^\mu - \theta_i \\ x_i^\mu = g(b_i^\mu) \end{cases}$$

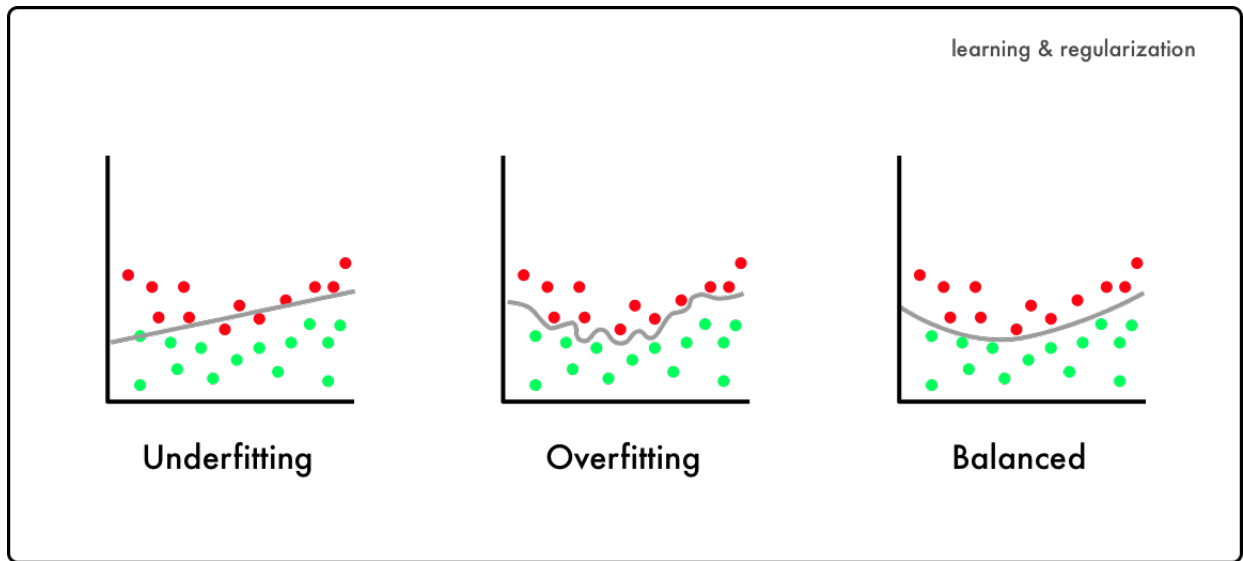
where  $b_i$  is called the *local field* for the  $\mu$ th pattern in the next layer, and the activation function calculates the vector in the next layer.  $i$  tells you how many neurons there are in the next layer. This method of update is called synchronous update which means that all neurons have been updated simultaneously. An alternative is to select an arbitrary neuron and just update that one only. That scheme is called asynchronous update.

A network with multiple layers can mathematically be described by

$$\begin{cases} V_j^\mu = g(b_j^\mu) & \text{with } b_j^\mu = \sum_k w_{jk} x_k^\mu - \theta_j \\ O_1^\mu = g(B_1^\mu) & \text{with } B_1^\mu = \sum_k w_{1k} x_k^\mu - \theta_1. \end{cases}$$

Here  $V_j^\mu$  denotes some layer of neurons and  $O_1^\mu$  denotes the *output layer*. The output layer is the last layer whose result becomes visible. This result should, if the network works correctly, equal the target. Whenever one checks how well the network has performed one subtracts the values of  $O_1^\mu$  with the targets.

In general it is not possible to say, how many layers are needed to solve a specific problem, and what is the minimal number of layers. The number of layers should be minimised as increasing the number of layers unnecessarily may lead to something called *Overfitting*. The goal for the network is to learn, generalise and find general trends from the given data. Having too many layers can lead to that the network will perfectly "understand" and predict for a particular set but it will be completely useless for other similar sets. [16].



The image depicts three different networks' possible states for one data set. When the network will have too few layers the network will find and make too few rules which will to that it will not correctly predict the output values for the data set. This is shown under "Underfitting". In the middle image we see a network have too many layers. We see that the network have correctly separated all output values. The problem here is that it is very sensitive for changes and for similar data sets it will not predict correctly. This is called "Overfitting". In the last image we have a nice number of layers. The network has successfully managed to separate the two output values and for some differences it will still be able to separate different output values. One says the network has found the general trend. Figure taken from source: [30]

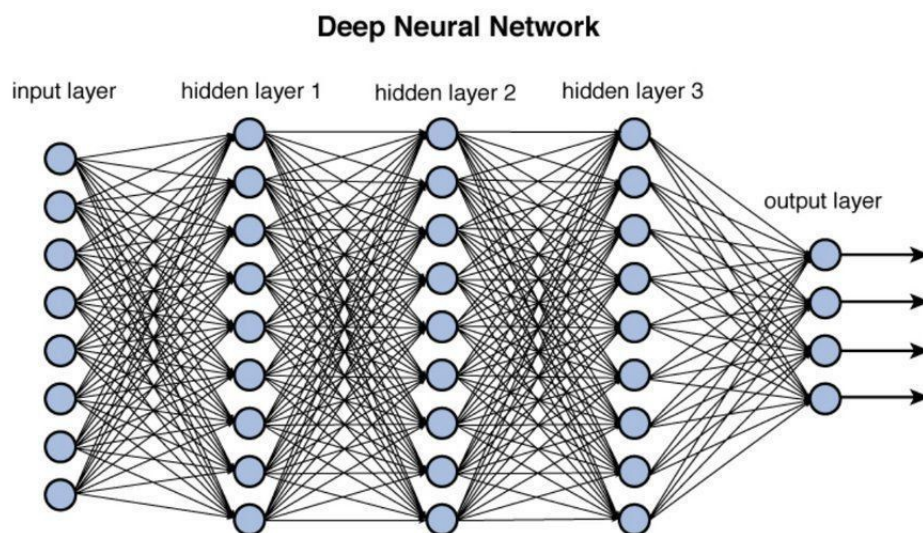


Figure 12.2 Deep network architecture with multiple layers.

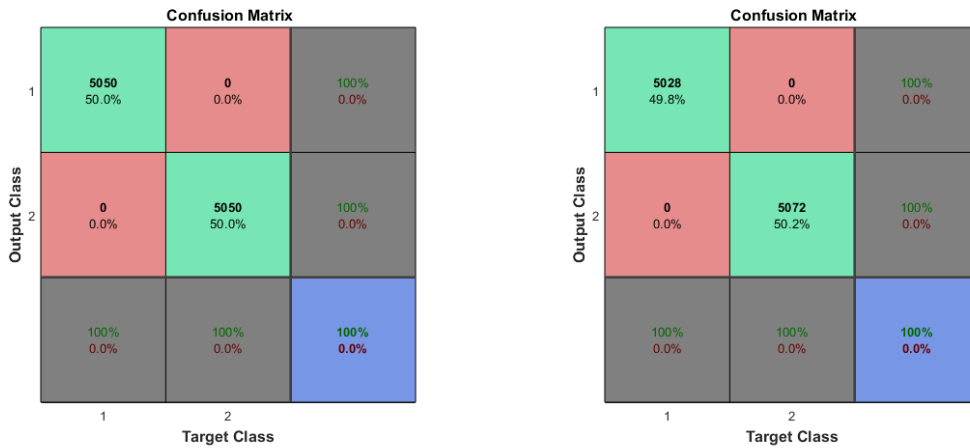
A simplified model of a deep learning neural network. In this task the neural network had, depending on the resolution of the Faraday spectrum, up to 100 neurons. As a standard modelled network there was 20 hidden neurons in each next layer, and there was one output, 1 or 0 (in this figure the output layer have instead four outputs). [30]

## Method, results and discussion

I simulated over 10 000 Faraday spectra representing polarised and not polarised sources. The data set of confirmed polarised sources is yet too small to work on. The simulated Faraday spectra were created with a Ricean noise<sup>2</sup> using a Gaussian (normal) number generator. In case of a not polarised source, the entire Faraday spectrum consisted of only random values (Ricean noise). Common values of noise for many Faraday spectra that I have been investigating were constrained around  $10^{-5}$ , which I then modelled the noise with the same value multiplied by the Ricean noise. In the case of a polarised source, the same procedure was repeated but an additional spike with the value of this spike fulfilled  $S/N > 6$  at a random bin.

Each spectrum was then assigned with a target (I assigned the Faraday spectra with a 1 if it represented a polarised source otherwise with 0). I simulated at first equally many Faraday spectra representing not polarised sources and Faraday spectra representing polarised sources. After a bit of examination networks with two layers and 20 neurons in each resulted in the network predicted correct target for every output. To make it more difficult for the network, I simulated at random with a uniform random generator, about 50% would represent a polarised source and the other 50% would represent the opposite. This also resulted in the network predicted correct target for every output with the same structure of the network.

Both approaches ended up with successful results. The network learned in about 20 seconds to distinguish all Faraday spectra. All outputs matched all targets correctly. This could be an indication that searching for polarised sources in radio polarisation data is ready use of neural networks.



Confusion matrices for both attempts using neural networks for simulated radio polarised data with Ricean noise. The score is perfect.

<sup>2</sup>Ricean noise is  $R = \sqrt{G_1^2 + G_2^2}$ , where  $G_1$  and  $G_2$  are Gaussian distributed values.

## The algorithm

### The algorithm

```

1 %% MyProgram – Script
2 clear all
3 fname = 'file_Sourcel_p.fits'; %Example file
4 fifi = fitsread(fname);
5 ffname='file_Sourcel_low_I_corr.fits';
6 fifl=fitsread(ffname);
7
8
9 %% IDENTIFYING AND FINDING THE CENTROIDS OF BLOBS/GALAXIES
10 clc
11
12 X=fifl; %fifl; %EX: Initialisation
13 J = imadjust(X, [0.009 0.01], []); %imadjust(X, [x, y], []); x
    =0.009, y=0.01
14 % x increases darkness in map and decides about numbers of
    sources, y increases brightness
15 BW=J;
16 figure(1)
17 imshowpair(J, fifl, 'montage')
18 [ii, jj]=find(BW); %FINDS COORDS FOR BLOBS, ii=ycoords, jj=
    xcoords
19
20 CC = bwconncomp(BW); %connects neighbour pixels, identifies
    them as blobs
21 s = regionprops(CC, 'centroid');
22 centroids = cat(1, s.Centroid);
23 figure(2)
24 plot(jj, ii, '. ') %MAP
25
26 %PLOTS EVERY SOURCE AND ITS CENTROID
27 stats = regionprops('table', CC, 'Centroid', ... %ALL RELEVANT
    INFO,
28     'Area')
29 Area=table2array(stats(:,1));
30 Centroid=table2array(stats(:,2));
31 xcoord=Centroid(:,1);
32 ycoord=Centroid(:,2);
33 sprintf('Number of blobs are: ')
34 NumberOfBlobs=size(Area,1)
35 hold on
36 title('Map with centroids')
37 xlabel('x – axis')
38 ylabel('y – axis')

```

```

39 plot(round(xcoord),round(ycoord),' ') %ROUNDED COORDINATES
40 %% FIND POLARISATION (COORDs/PIXELs) BASED ON THRESHOLD THEN
    PRODUCE F(PHI)
41 clc
42
43 x = 1:size(fifi,3);
44 M=zeros(length(x), sum(Area));
45 H=zeros(length(x), sum(Area));
46 count = 0;
47 vdistr=zeros(size(fifi,2), size(fifi,1));
48 % THE FOLLOWING SYNTAX WORKS IN MATLAB version 2017 AND LATER
49 %-----
50 %fitsdisp(fname,'Mode','full');
51 %info = fitsinfo('fname');
52 %information=info.PrimaryData;
53 %Cell=information.Keywords; %CELL WITH ALL INFORMATION FROM THE
    HEADER
54 %format long
55 %CDelt3 = Cell{find(strcmp(Cell, 'CDELTA3')),2};
56 %dStep=CDelt3;
57 %-----
58 dStep=0.3; %Manually selecting dphi
59
60 fprintf(" # Region file format: DS9 version 4.1 global color=
    green dashlist=8 3 width=1 font="helvetica 10 normal roman"
    select=1 highlite=1 dash=0 fixed=0 edit=1 move=1 delete=1
    include=1 source=1
61 image")
62 tic
63 for i=1:sum(Area) %ITERATE OVER RELEVANT PIXELS
64
65     for k = 1:length(x) %ITERATE OVER PHI
66
67
68         M(k,i) = conv2(fifi(ii(i),jj(i),k), ones(4,4), 'same')
            ./ conv2(ones(size(fifi(ii(i),jj(i),k))), ones(4,4),
                'same'));
69
70     end
71
72     for k=[1:round(-4/dStep + length(x)/2), round(length(x)/2+2/
        dStep):length(x)]
73
74
75         if (M(k,i) > (mean(M(:,i)) + 6 std(M(:,i)))) %S/N > n
76

```



```

77         formatSpec='circle(%d,%d,2.2222) \n'; % Image
           coordinates for a region file
78
79         A1=jj(i);
80         A2=ii(i);
81         A3=i;
82         A4=(x(k)-size(fifi,3)/2) dStep;
83         vdistr(ii(i),jj(i))=A4;
84         sprintf(formatSpec,A1,A2)
85         count = count + 1;
86         end
87
88     end
89
90
91
92 end
93 toc
94 formatSpec='Number of found polarised sources are: %d';
95 A=count;
96 fprintf(formatSpec,A)
97 ax1=axes;
98 mesh(ax1,fif1)
99 view(2)
100 ax2=axes;
101 contour(ax2,vdistr)
102 linkaxes([ax1 ax2])
103 ax2.Visible = 'off';
104 ax2.XTick = [];
105 ax2.YTick = [];
106 cmap=colormap(ax1,gray);
107 newmap=imadjust(cmap,[0.005 0.15]);
108 colormap(ax1,newmap)
109 colormap(ax2,'Jet')
110 %set([ax1,ax2],'Position',[.17 .11 .685 .815]);
111 axis auto
112 cb2 = colorbar(ax2,'Position',[.88 .11 .0675 .815]);
113 %hold on
114 %hold off
115
116 % REVERSES THE X-AXIS AND KEEPS THE IMAGE THE SAME
117 figure(3)
118 hold on
119 im = image('XData',[25 45], 'YData',[45 50], 'CData', fif1,
           'CDataMapping','scaled');
120 im.CData = fliplr(im.CData)

```

```
121 colormap(newmap)
122 colormap(ax2, 'Jet')
123 set(gca, 'xdir', 'reverse')
124 AxesH = gca;
125 axis(AxesH, 'tight');
126 hold off
```

### The network

```
1 %% MACHINE LEARNING – CLASSIFICATION TASK
2
3 clc, clear all
4 N = length(x); % INTERVAL FOR ENTIRE FARADAY SPECTRUM
5 %rng default; %FOR REPRODUCIBILITY
6 normQ = randn(1,N); % NORMAL (GAUSSIAN) DISTRIBUTION (MEAN) =
    0, STANDARD DEVIATION (SIGMA) = 1
7 normU = randn(1,N);
8 P=sqrt(normU.^2+normQ.^2); %RICEAN DISTRIBUTION, NOISE VALUES
9 NumberOfSimulatedFaradaySpectra=100N;
10 limit1=1e-4;
11 limit2=1e-5; %CONSTRAINTS
12
13 n=6; %S/N > n
14
15 LargeMatrix=zeros(N,N 100); %INTIALISING SIMULATED FARADAY
    SPECTRA MATRIX
16 LargeMatrixTarget=zeros(2,NumberOfSimulatedFaradaySpectra); %
    INTIALISING TARGETS MATRIX
17
18 for i=1:(size(LargeMatrix,2)/2) %CREATING SIMULATED NON-
    ACCEPTABLE FARADAY SPECTRA AND CORRESPONDING TARGETS
19     vector = P 1 e-6;
20     LargeMatrix(:,i) = vector;
21     LargeMatrixTarget(1,i)=0;
22     LargeMatrixTarget(2,i)=1;
23 end
24
25 for i = (size(LargeMatrix,2)/2+1) : size(LargeMatrix,2) %
    SIMULATED ACCEPTABLE FARADAYSPECTRA AND TARGETS
26     vector = P 1 e-6;
27     LargeMatrix(:,i) = vector;
28     random = mean(vector)+n std(vector);
29     phi_value = randi(N);
30     LargeMatrix(phi_value,i)=random;
31     LargeMatrixTarget(1,i)=1;
32     LargeMatrixTarget(2,i)=0;
33 end
```

```

34
35 inputs = LargeMatrix;
36 targets = LargeMatrixTarget;
37 %%
38 clc , clear all
39 %N = length(x); % INTERVAL FOR ENTIRE FARADAY SPECTRUM/NEURONS
    IN PATTERN
40 %rng default; %FOR REPRODUCIBILITY – OPTIONAL
41 normQ = randn(1,N);
42 normU = randn(1,N);
43 P=sqrt(normU.^2+normQ.^2); %RICEAN DISTRIBUTION, NOISE VALUES
44 NumberOfSimulatedFaradaySpectra=100N;
45
46 n=6; %S/N > n
47 LargeMatrix=zeros(N,N 100); %INITIALISING SIMULATED FARADAY
    SPECTRA MATRIX
48 LargeMatrixTarget=zeros(2,NumberOfSimulatedFaradaySpectra); %
    INITIALISING TARGETS/RESULTS MATRIX
49 for i = 1: size(LargeMatrix,2)
50     vector = P 1 e-6;
51     LargeMatrix(:,i) = vector;
52     x = round(rand(1,1)); % coin flip , 50 percent 1 or 0
53     if (x==1) % Simulate a Faraday spectrum representing a
        polarised source
54         random = mean(vector)+n std(vector);
55         phi_value=randi(N);
56         LargeMatrix(phi_value,i)=random;
57         LargeMatrixTarget(1,i)=1;
58         LargeMatrixTarget(2,i)=0;
59     end
60     if (x==0)
61         LargeMatrixTarget(1,i)=0;
62         LargeMatrixTarget(2,i)=1;
63     end
64 end
65
66 inputs = LargeMatrix;
67 targets = LargeMatrixTarget;
68 %% RUN NETWORK
69
70 % Create a Pattern Recognition Network
71 hiddenLayerSize = [20 20]; %EXAMPLE – 2 LAYERS, 20 NEURONS IN
    ONE EACH
72 net = patternnet(hiddenLayerSize);
73
74

```

```
75 % Set up Division of Data for Training , Validation , Testing –  
    RECOMMENDED  
76 net.divideParam.trainRatio = 70/100;  
77 net.divideParam.valRatio = 15/100;  
78 net.divideParam.testRatio = 15/100;  
79  
80  
81 % Train the Network  
82 [net, tr] = train(net, inputs, targets);  
83  
84 % Test the Network  
85 outputs = net(inputs);  
86 errors = gsubtract(targets, outputs);  
87 performance = perform(net, targets, outputs);  
88 %View the Network  
89 figure, plotconfusion(targets, outputs)
```